Metal-Organic Frameworks Meet Polymers: From Synthesis Strategies to Healthcare Applications

Anivind Kaur Bindra, Dongdong Wang, and Yanli Zhao**

Dr. A. K. Bindra, Prof. D. Wang, Prof. Y. L. Zhao
School of Chemistry, Chemical Engineering and Biotechnology
Nanyang Technological University
21 Nanyang Link, Singapore 637371, Singapore
E-mail: zhaoyanli@ntu.edu.sg

Prof. D. Wang
Hefei National Laboratory for Physical Sciences at Microscale
University of Science and Technology of China
Hefei 230026, P. R. China
E-mail: wangdd13@ustc.edu.cn

Keywords: hybrids • metal-organic frameworks • nanomedicine • polymers • theranostics

Abstract: Metal–organic frameworks (MOFs) have been at the forefront of nanotechnological research for the past decade owing to their high porosity, high surface area, diverse configurations, and controllable chemical structures. They are a rapidly developing class of nanomaterials that are predominantly applied in batteries, supercapacitors, electrocatalysis, photocatalysis, sensors, drug delivery, and gas separation, adsorption, and storage. However, the limited functions and unsatisfactory performance of MOFs resulting from their low chemical and mechanical stability hamper further development. Hybridizing MOFs with polymers is an excellent solution to these problems, because polymers—which are soft, flexible, malleable, and processable—can induce unique properties in the hybrids based on those of the two disparate components while retaining their individuality. This review highlights recent advances in the preparation of MOF–polymer nanomaterials. Furthermore, several applications wherein the incorporation of polymers enhances the MOF performance are discussed, such as anticancer therapy, bacterial elimination, imaging, therapeutics, protection from oxidative stress and inflammation, and environmental

remediation. Finally, insights from the focus of existing research and design principles for mitigating future challenges are presented.

1. Introduction

MOFs also known as coordination polymers, are three-dimensional (3D) porous materials comprising inorganic metal nodes or clusters—termed secondary building units—that are interlinked with rigid multitopic organic linkers.[1] The specific geometry and functionality of the organic ligands and the characteristics of the metal ions such as size, geometry, and association constants are crucial in determining the crystallinity of MOF particles. Owing to advances in the field of organic–inorganic hybrid porous frameworks, various MOFs such as zeolite imidazolate frameworks (ZIFs);[2–4] HKUST-1 (HKUST: Hong Kong University of Science and Technology);[5–7] UiO-66 (UiO: University of Oslo);[8,9] MIL-100[10] and MIL-101[11,12] (MIL: Matériaux de l′Institut Lavoisier); and Prussian blue analogs[13,14] have been developed and explored in recent years.[15] Owing to their tunable particle size, morphology, and surface area, MOF-based systems with diverse metal centers and organic ligands have been used for gas adsorption, storage, and separation;[16] catalysis;[17] sensing;[18] biomedical engineering;[19] toxin removal;[20] battery devices[21–23] and other purposes.[24]

To enhance their existing functionalities and to introduce new characteristics, MOFs have been combined with an array of materials such as silica, graphene, polymers, biomacromolecules, and metal clusters and nanoparticles.[25–29] Among the numerous MOF-based hybrids, MOF–polymer nanocomposites have garnered considerable attention as they can exploit the benefits of both the MOF and polymer structures.[30] In most native polymeric systems, polymer chains are randomly arranged in the solution phase. However, in polymer-encapsulated MOF systems, the number, chemical orientation, and environment of polymer chains can be precisely controlled and evaluated. Moreover, encapsulation of synthetically prepared functional polymers could lead to the development of host–guest-type supramolecular hybrids with interesting properties.

The coordinative interactions in native MOFs are thermodynamically stable but kinetically labile because they are weaker than covalent bonds (100–300 and 200–800 kJ mol^{-1}, respectively).[31,32] Interestingly, the materials originating from polymer-ligand-bearing MOFs exhibit particularly enhanced chemical, thermal, and mechanical stability; hierarchical porosity; and morphological and crystal size control. However, in the presence of water molecules, the coordinative interactions between the metal ions and ligands of constituent clusters are weakened owing to hydrolyzation, leading to the collapse of the MOFs. A

classical approach to enhance the chemical stability of MOFs involves coating a hydrophobic polymer onto the external MOF surface.[33,34] For instance, the diffusion rate of water molecules into the HKUST-1 pores has been reduced by encapsulating it with polystyrene microspheres, inhibiting its structural transformations. To elucidate the impact of polymers on MOF pore stabilization and thermal stability, Uemura et al. selected $[Co_2(NDC)_2(BiPy)]_n$ (NDC: 2,6-naphthalene dicarboxylate; BiPy: 4,4'-bipyridine) as the MOF host with a two-fold interpenetrated structure comprising flexible one-dimensional (1D) nanochannels.[35] After the partial in situ polymerization of vinyl monomers within the channels, the polymer chains restricted the mobility of the network, leading to a thermally stable (>200 °C) open microporous state. The relative stiffness of the framework caused the local deformation to propagate through adjacent channels, and several empty nanochannels were available for significantly enhanced gas absorption.

In terms of bio-related applications, MOFs and polymers have been integrated and applied as intelligent disease diagnosis, monitoring, and therapy agents, primarily because of the flexibility offered by the engineered MOFs in terms of their metal centers and conjugation of polymers.[36–43] Yang et al. reported COOH-coordinated nanoscale metal–organic particles (NMOPs) self-assembled from Mn^{2+} ions and IR825 bridging ligands coated with polydopamine (PDA) and polyethylene glycol (PEG).[36] The prepared Mn-IR825@PDA-PEG NMOPs exhibited efficient T_1-weighted magnetic resonance imaging (MRI) and remarkable photothermal-conversion-enabled tumor elimination in vivo. Detection and sensing are also critical in clinical as well as environmental settings to accurately determine the concentrations of biomarkers or toxins. Deep et al. doped a conducting polyaniline (PANI) substrate with an NH_2-BDC linker (NH_2-BDC: 2-aminobenzene-1,4-dicarboxylic acid), coated it with a silica-modified Cu-based MOF ($Cu_3(BDC)_2$), and then conjugated it with antibodies to form a conductometric immunosensor—antibody/$Cu_3(BTC)_2$@SiO_2/BDC-PANI—for detecting the widely used pesticide atrazine.[37] Thin nanofiber films of BDC-PANI served as a homogenous base, and the inherent conductivity improved the conductance, with the detection limit as low as 0.01 nM.

Several reviews have recently detailed the diverse applications of MOFs such as environmental protection,[38] catalysis,[39] energy storage,[40] battery development,[41] sensing and detection, microbial eradication, and anticancer therapy.[1] The present review is aimed at exploring recent advances in the integration of MOFs and polymers for healthcare applications (**Scheme 1**). Initially, the synthesis methods used for rational design of MOF–polymer hybrids are discussed with relevant examples. Subsequently, medical

applications such as cancer therapeutics, involving responsive drug delivery and phototherapies, are highlighted. Furthermore, other applications such as bacterial elimination, sensing, biomedical imaging, environmental toxin removal, and cellular protection from reactive oxygen species (ROS) and inflammation are scrutinized. Finally, certain conclusions and prospects of MOF–polymer hybrid development as a fast-evolving research frontier are discussed.

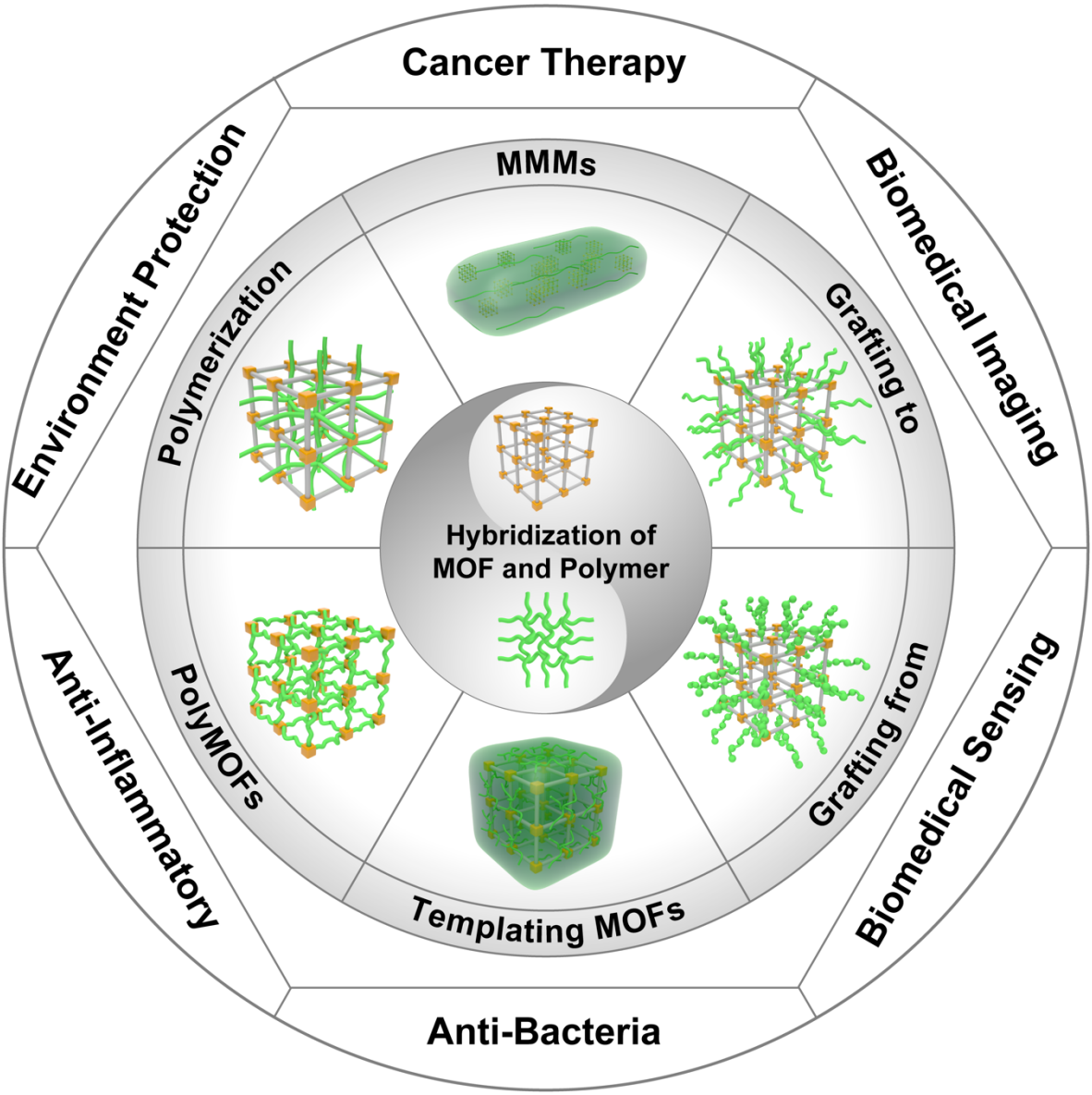

Scheme 1. Schematic illustrating MOF–polymer hybridization for healthcare applications such as cancer therapy, biological imaging, biological sensing, antibacterial treatment, anti-inflammation, and environmental protection.

2. MOF–Polymer Hybridization Strategies

MOF–polymer integration has inspired the development of new composite materials exhibiting more diverse, favorable properties than those of the individual MOF or polymer. Several research groups have reported elegant methods to synthesize MOF–polymer hybrids, which have helped enhance the practical applicability of MOFs. Studies have been conducted on synthesizing polymers in and around MOF crystallites using methods such as fabrication of mixed-matrix membranes (MMMs), preparation of polymers covalently 'grafted-to' and 'grafted-from' the MOF surface, utilization of polymers as templates and ligands for MOF growth, and introduction of polymers into the MOF nanochannels.

2.1. Mixed-Matrix Membranes. As a highly effective strategy for incorporating rigid porous solids such as zeolites, carbons, and MOFs into flexible form factors, MMM fabrication offers cumulative advantages arising from the disparate components. MOF-based MMMs are predominantly used to separate gases with similar sizes and properties, such as O_2, N_2, CO_2, and CH_4, because of their improved selectivity and permeability. The selectivity and permeability of pure polymeric membranes are inversely correlated; this is termed the Robeson upper bound.[44] The introduction of organic–inorganic materials such as MOFs into natural polymers can increase the Robeson-upper-bound limits, which has stimulated research in this field.

Two types of MMMs—conventional and covalently connected MMMs—can be synthesized. In conventional MMM synthesis, which involves dispersion of a simple solution and casting, a dissolved polymer solution is added to an MOF-containing volatile solvent and mixed until homogenization is achieved. A freestanding MOF-based MMM film is obtained after subjecting the MOF–polymer mixture (denoted as MOF 'ink') to film casting and solvent evaporation. However, the membrane performance is hindered by incompatibility between the MOF and polymer components, leading to MOF–polymer interfacial defects. To amplify the interactions, functionalized MOFs have been combined with glassy polymers, such as poly(methyl methacrylate) (PMMA), polysulfone (PSF), and polyimide (PI). For example, using amine functionalization, Chen and Kong integrated the CAU-1-NH_2 MOF (CAU: Christian Albrechts University) with PMMA to form an MMM, which was highly selective for H_2 over CO_2 and exhibited a H_2 permeability that was several times higher than that of pure PMMA.[45] Urban et al. used MOF loadings of up to 50 wt% to combine UiO-66-NH_2 and PSF and achieved high selectivity for CO_2 over CH_4 and N_2.[46] A common drawback of MMMs with high MOF loadings (>40%) is low dispersibility, resulting in sedimentation and subsequent generation of nonselective macrovoids at the MOF–polymer

interface. To tackle this issue, Cohen et al. prepared 67%-MOF-loaded freestanding MMMs using polyvinylidene fluoride (PVDF) films and diverse MOFs such as UiO-66, HKUST-1, MIL-101, MIL-53, and ZIF-8 (**Figure 1a**).[47] The macroscopic-defect-free MMMs were prepared using preformed MOFs dispersed in a solvent containing the PVDF polymer solution. Li et al. fabricated PI-brush-modified MMMs, which exhibited improved interfacial compatibility, increased ductility (472%), as well as high MOF loading (88%) and enhanced gas-separation capabilities.[48] Assisted by the abundant amino groups on the surface of UiO-66-NH_2, the PI polymer brush was grown to fabricate the MMM without adding the PI matrix, resulting in enhanced interfacial adhesion and particle dispersibility.

2.2. Covalent Polymer Grafting. The absence of specificity and precise control at the MOF–polymer interface can be exploited to covalently attach polymers to the MOF surface. The surface attachment of polymers via specific groups considerably affects their interactions with the surroundings and helps manifest new properties such as improved robustness, elevated compatibility, and stability. Additionally, the method for obtaining MOF-tethered polymers is popular owing to its simplicity. 'Grafting-to' and 'grafting-from' are the two common approaches adopted to covalently link the components.

2.2.1. 'Grating-To' Approach: Polymers can be grafted onto the MOF surface using two methods. The first approach involves using presynthesized polymers containing complementary groups such as carboxylic acids and thiols that can be attached to the MOF surface, whereas the second strategy involves presynthesizing MOFs from reactive functional groups with species such as C=C and N_3. For example, various polymers were grafted onto Gd-based MOFs in initial studies.[49,50] Diverse hexylamine-appended homopolymers with varying chemical and structural characteristics—poly(*N*-isopropylacrylamide) (PNIPAM), polystyrene (PS), poly(2-(dimethylamino)ethyl methacrylate) (PDMAEA), poly(((poly)ethylene glycol) methyl ether acrylate) (PPEGMEA), and poly(acrylic acid) (PAA)—were prepared via reversible addition–fragmentation chain transfer (RAFT) and grafted onto the Gd-MOF surfaces, resulting in finetuned and tailored longitudinal relaxivity (r_1) and transverse relaxivity (r_2) values. Subsequently, Zimpel et al. covalently modified an iron-cluster containing MIL-100(Fe) appended with a carboxylic acid to combine with poly(ethylene glycol) (PEG)-NH_2 (M_w 5000) and the Stp 10-C (oligoamino amide) bifunctional linker (**Figure 1b**).[51] Fluorescence correlation spectroscopy and ultraviolet–visible spectroscopy were employed to determine the extent and amount of surface grating. A major advantage of this approach is that it permits the use of various chemical and

polymer characterization techniques to effectively verify the polymer structure and properties prior to the attachment.

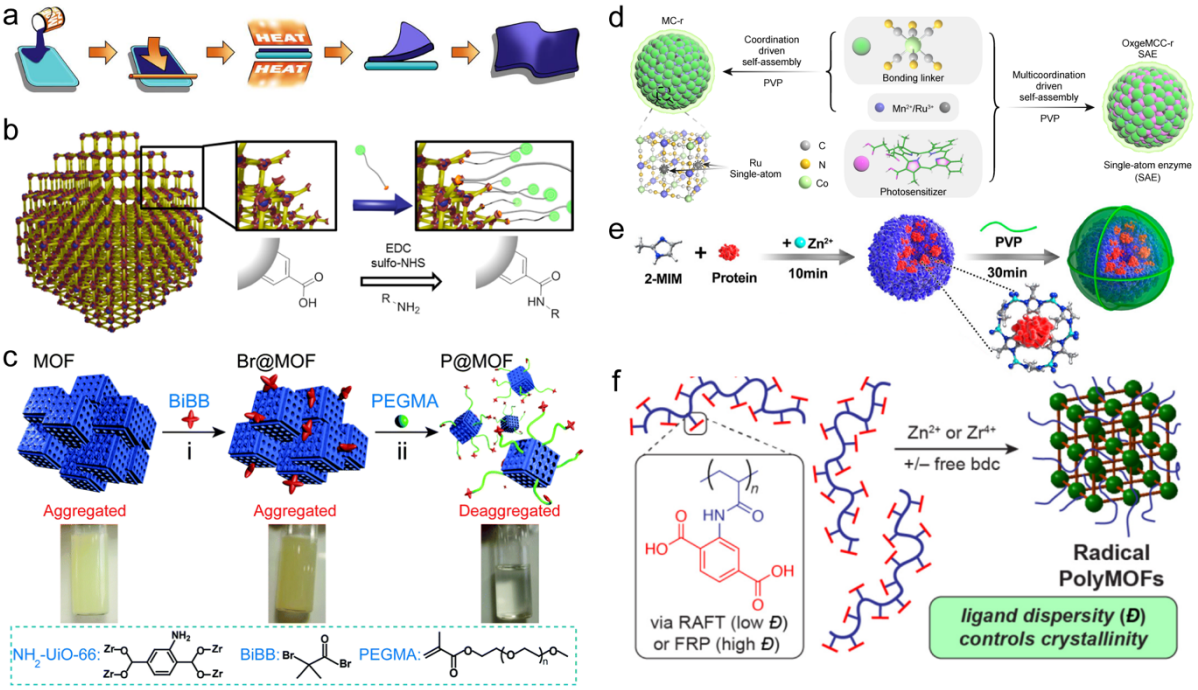

Figure 1. Strategies for MOF–polymer integration. (a) Schematic illustrating the synthesis of MOF-based MMMs using the casting method. Reprinted with permission.[47] Copyright 2022, Wiley-VCH. (b) MIL-100(Fe) coated using the polymer 'grafting-to' approach via a carbodiimide-mediated reaction. Reproduced with permission.[51] Copyright 2016, American Chemical Society. (c) UiO-66 coated with a PEGMA polymer brush using the 'grafting-from' approach. Reproduced with permission.[52] Copyright 2015, Royal Society of Chemistry. (d) Preparation of OxgeMCC-r appended with Ru single-atoms and encapsulated with polyvinylpyrrolidone (PVP). Reproduced with permission.[57] Copyright 2020, Springer Nature. (e) Fabrication of PVP-coated BSA@ZIF8 nanoparticles. Reproduced with permission.[65] Copyright 2018, American Chemical Society. (f) Schematic describing the synthesis of 'polyMOFs' MOF-5 and UiO-66 using radical polymerization techniques. Reproduced with permission.[72] Copyright 2021, American Chemical Society.

2.2.2. 'Grafting-From' Approach: This strategy, also denoted as post-synthetic polymerization, is a reliable and robust approach for generating MOF–polymer hybrids with high polymer densities. Other advantages include molecular weight adjustment, low dispersity indices, and hydrolytically stable architectures. In this approach, the MOF surface is typically functionalized with initiating groups specific to the polymerization type. Webley et al. prepared PEG@UiO-66-NH_2 via atom transfer radical polymerization (ATRP) of the

macromonomer (polyethylene glycol) methyl ether methacrylate (PEGMA) onto a bromo-surface-modified MOF (**Figure 1c**).[52] Highly water-dispersible core–shell particles (poly@MOF) with an optimal size of 70 nm were produced compared to the heavily aggregated 1-μm-sized bare UiO-66-NH_2 particles. However, the the heavy-polymer-grafted MOF surfaces significantly reduced the surface area of the mesoporous MOFs. Thus, an IRMOF-3 shell was constructed around the MOF-5 core to circumvent pore clogging, which helped both in providing the initiating sites and mitigating the pore blockage.[53] However, this approach may pose another challenge in terms of enabling cleaving and isolation of attached polymer chains for full characterization.

2.3. Polymer-Templated MOF Growth. Supramolecular templating for mesoporous structures has been inspired by established silica-preparation methods.[54,55] Essentially, this approach involves co-assembling structure-directing agents (SDAs) such as nonionic polymers into ordered mesoscale arrays through various noncovalent interactions. Commonly used pluronic nonionic polymers containing poly(ethylene oxide) (PEO) and poly(propylene oxide) (PPO) blocks are potent SDAs.[56] However, the polyether functionalities of pluronic polymers exhibit limited interactions with the metal nodes and organic ligands for constructing a supramolecular assembled network structure. Therefore, another polymer—PVP—is used to enhance coordination with the SDAs. The presence of multiple pyrrolidone groups in the structure can stabilize the metal ions. In several studies conducted by our group, PVP was used as a surfactant to link several metal ions and the photosensitizer chlorin e6 via coordinative interactions (**Figure 1d**).[57] Nonionic polymers with tunable polymer composition and architectures, such as double-hydrophilic block copolymers (DHBCs), are another class of polymers that can modulate MOF crystal growth and morphogenesis. In DBHCs, one hydrophilic segment imparts solubility, whereas the other modulates polymer–mineral interactions. In an innovative study, Hwang et al. developed Zn- and Cu-based 3D mesocrystals with adjustable anisotropic shape, size, aspect ratio, morphology, and structures.[58] Poly(ethylene oxide)-*block*-poly(methacrylic acid)—a DHBC—assisted in maintaining kinetic and thermodynamic balance during the MOF mesocrystal formation. The carboxylic-acid-appended functionality in the DHBC regulated the morphology by modulating the coordination, whereas the ethylene oxide block induced particle stabilization by controlled aggregation, inducing meso-assembly.

2.4. Polymers in MOF Nanochannels. Research on the preparation of MOF–polymer hybrids has primarily been fueled by the ease of post-modification strategies with pre-formed polymers for MOFs. Techniques such as melt processing, solution-mediated incorporation, and polymer self-assembly with concomitant MOF growth have been reported. Uemura et al. reported a melt-processing technique wherein PEG chains with varying molecular weights (M_w = 400–3000), long-chain alkanes (n = 20–40), and polymethylpropylsilane (M_n = 3600) were processed into composites with MOFs of varying pore sizes.[59–61] Briefly, the synthesis involved immersing the host MOFs in a solvent containing the polymer moiety and subsequently evaporating the solvent above the polymer-melting temperature. Thermal transition of the polymer was governed by two important characteristics: narrow pore size and high polymer molecular weight. Molecular dynamics (MD) simulations and density functional theory (DFT) studies indicated that the polymers were destabilized within the small, confined pores of the host MOFs. Polymers as well as proteins have been utilized for biomacromolecular immobilization. However, impregnating proteins into pre-synthesized materials creates issues such as large pore sizes and low loading capacities.[62,63] Biomimetic mineralization allows the preparation of protein-encapsulated MOFs with narrow pore sizes to enhance the activity, functionality, and stability of proteins.[64] Chen et al. prepared PVP-coated BSA@ZIF-8 particles (BSA: bovine serum albumin) by pre-mixing a protein solution with methylimidazole moieties, and then adding a metal salt solution (**Figure 1e**).[65] The BSA concentration in the seeded clusters directly impacted the growth kinetics, enabling the formation of larger crystals with a BSA loading of ~91%. Using surface properties as the driving force, Chen et al. demonstrated an amino-acid-boosted one-pot embedding strategy to encapsulate 12 distinct proteins into MOFs such as ZIF-8 and KHUST-1.[19] The prenucleation clusters around the proteins, which enabled MOF generation, were driven by metallothionein interactions between Zn^{2+} and the abundant cysteine amino acids. Furthermore, with PVP as a capping agent, the amide-bond-enriched hydrogen bonding interactions yielded a strong PVP/protein complex with a myoglobin loading of ~18.2 wt%. Thus, in addition to enabling high protein inclusion, MOF-coated proteins could serve as a platform for achieving rapid encapsulation, preserving protein activity, preventing enzyme degradation, and realizing controlled release.[66]

2.5. Polymer Ligands for MOF Growth. Bottom-up polyMOF formation is a relatively nonconventional method of preparing MOF–polymer composites, wherein instead of the small-molecule-based organic linkers, the polymer is coordinated to metal nodes. The most

remarkable feature of polyMOF composites is the function of amorphous polymers as the organic building blocks. However, the formation of highly crystalline MOF architectures using polymers seems unfeasible from conventional wisdom, which suggests that the product would be a disorganized, amorphous linked solid. Moreover, the unmet kinetic and entropic requirements of polymers would result in chain entanglements and structural irregularities. Inspired by the synthesis of IRMOF-1 reported by Yaghi et al., Cohen et al. prepared derivatives using the crosslinked, polymeric 1,4-benzene dicarboxylic acid ligand (H_2BDC).[67,68] A series of polymer ligands with different methylene spacers (CH_2 = 5–8) was prepared via step-growth polymerization. Spherical particles with intergrown crystalline superstructures having regular facets were formed, which differed from the regular cubic particles in the highly crystalline IRMOF with specific spacer lengths (7 and 8). The presence of multiple nucleation sites on the polymer ligands coordinating to Zn^{2+} led to the simultaneous growth of individual crystals and shared ligands. Moreover, the hybrid structure exhibited improved stability with minimal change in the crystallinity upon exposure to air for three days. Furthermore, Zn-pbdc-8a recovered to its original state after the unstable crystals were treated at 60 °C in dimethylformamide (DMF) for an hour, owing to the increased hydrophobicity caused by the polymer ligand. This seminal study created vast opportunities to enable the preparation of polyMOFs with emergent properties.

Cohen et al. further explored the possibility of preparing polyMOFs using other Zn-, Zr-, and Cu-based MOFs.[69] A pillaring pyridine-based mixed-ligand approach was adopted to enhance aqueous stability by replacing the $CH_3OC_2H_4$ chains directed toward the pore channels.[70] To gain insight into the architectural constraints of the polymer backbone and linker spacing that govern polyMOF formation, Maurin et al. conducted studies by combining DFT calculations and solid-state nuclear magnetic resonance spectroscopy.[71] PolyIRMOF-1 was found to be more accommodating to differently numbered methyl spacer groups on the same polymer backbone and less constrained than pristine polyUiO-66. These molecular modelling approaches, which have been employed to probe the internal architecture of polyMOFs, help expand the overall understanding of the synergistic effects of polymers and MOFs. In an interesting approach to synthesize the MOF-5 (Zn) and UiO-66 (Zr) polyMOFs, Johnson et al. prepared high- and low-dispersity polymers (with benzene dicarboxylic acid linkers) through free-radical polymerization (FRP) and RAFT, respectively (**Figure 1f**).[72] The FRP-based polymer ligands enabled the formation of properly oriented crystalline polyMOFs. Therefore, ligand dispersity was found to be closely related to the polyMOF crystallinity.

3. MOF–Polymer Hybrids: Interactions at Biointerfaces

Similar to the interactions exhibited by other types of nanomaterials in biological systems, those between nanoMOFs and their immediate environment play a significant role in living systems. Functionalization of nanoMOFs is a rational approach to controlling interactions between MOFs and biointerfaces. For instance, Zimpel et al. screened diverse polymers such as positively charged [branched polyethylene imine (BPEI) and the poly(amidoamine) (PAMAM) dendrimer G4], negatively charged [polyglutamic acid (PGlu) and PAA], neutral (PEG and polysorbate 20, Tween), and block copolymers [polyglutamate-*b*-polysarcosine (PGlu-PSar)] to gauge their ability to link with Zr-*fum* MOFs (**Figure 2**).[73] Various formulations of the prepared Zr-*fum*@Poly NPs were subsequently studied based on their physiochemical properties such as zeta potential, colloidal stabilization, protein binding, and intracellular interactions. The nature of the polymer binding to Zr-*fum* was verified by thermogravimetric analysis (TGA) and Brunauer–Emmett–Teller (BET) surface area evaluation. The negatively charged polymers—PGlu and PAA—exhibited increased weight loss in the TGA and decreased BET surface area, indicating enhanced polymer attachment. In terms of nanoparticle agglomeration, the Zr-*fum* MOFs coated with the positively and negatively charged polymers agglomerated at pH values near the isoelectric point because of weak electrostatic repulsion. However, the Zr-*fum* coated with the amphiphilic polymer PGlu-PSar, which coordinated via PGlu, exhibited enhanced colloidal stability with 130-nm-sized particles, which was maintained from a pH of 4 to 8 (zeta potentials (ZP): +25 and −12 mV, respectively), with the isoelectric point at 5.8. Moreover, PGlu-PSar was inert to bloodstream proteins such as albumin and IgG. Flow cytometry and confocal laser scanning microscopy (CLSM) were employed to study cellular interactions. The strong interactions exhibited by the positively charged polymer coatings resulted in aggregation at the cell membranes with less endocytosis. Fluorescence signals were observed for the negatively charged polymer coatings in the presence of the cytosol. Therefore, this comprehensive study recognized the interplay between the nanoMOF surfaces and biointerfaces, which could direct the design of functionalized MOFs.

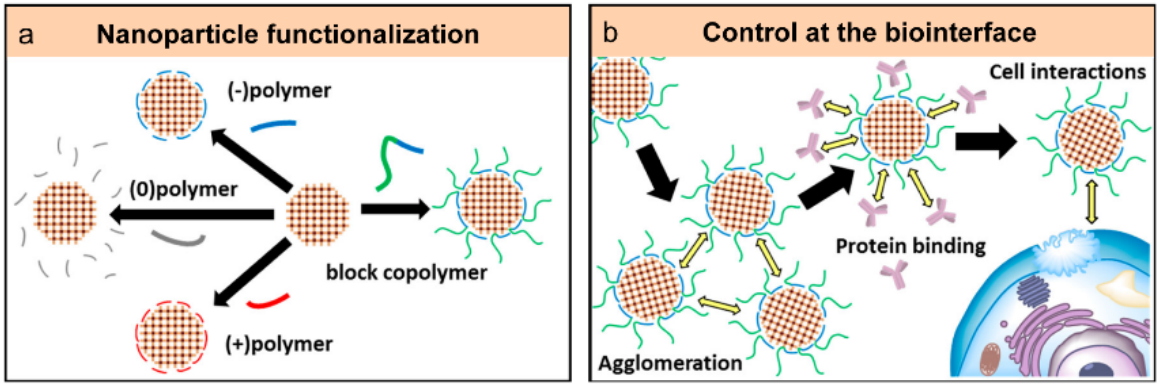

Figure 2. Schematic illustrating the (a) binding and surface coating of Zr-*fum* with charge-classified block copolymers (negative, neutral, positive, and hybrids at pH 7) and (b) investigation of physiochemical parameters that control colloidal stabilization, protein interaction, and cellular encapsulation. Reproduced with permission from ref [73]. Copyright 2019, American Chemical Society.

4. Applications of MOF-Polymer Hybrids

4.1. Anticancer Therapy

4.1.1. Responsive Drug Delivery. Chemotherapy is among the main lines of cancer treatment in clinical settings. However, it is often not encouraged owing to limitations such as nonspecific distribution, dose-limiting side effects, and drug resistance. Nanoscale MOF–polymer hybrids can act as smart materials to load and release drug cargos in response to various stimuli such as pH, ions, temperature, and light. Wei et al. modified hierarchically porous $UiO\text{-}66\text{-}NH_2$ with N,N-((((oxybis(methylene)bis(1,3-dioxolane-4,2-diyl))bis(oxy))bis(ethane-2,1-diyl))bis(2-methylacrylamide) (OEAM) to encapsulate cisplatin and doxorubicin (DOX) in the MOF matrix and polymer shell, respectively, for combination therapy.[74] The synthesized UiO was chemically modified with methacrylic acid to initiate the OEAM coating, which served as an acid-labile crosslinker for pH-responsive drug release. Surface charge reversal by the crosslinking polymer imparted remarkable stability, degradability in acidic conditions, and synchronous drug release. More importantly, nuclear accumulation and deep penetration were achieved in multidrug-resistant MCF-7/ADR (adriamycin)-inoculated tumors in vivo.

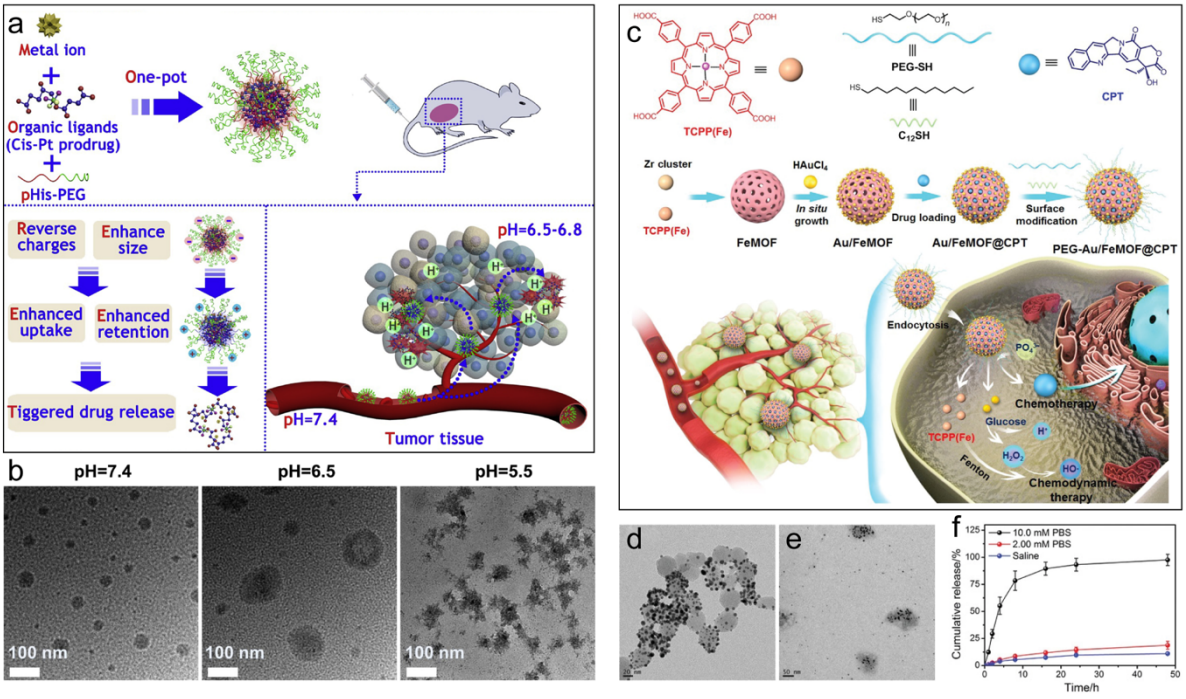

Figure 3. (a) Schematic illustrating the preparation of cisplatin-loaded one-pot PEG-modified NCP Hf/TCPP@pHis-PEG and its therapeutic action in an acidic tumor microenvironment (TME). (b) Transmission electron microscopy (TEM) images obtained using PBS with different pH values after incubation for 60 min. Reproduced with permission.[75] Copyright 2018, Elsevier. (c) Schematic illustrating the preparation of PEG-Au/Fe-MOF@CPT NPs via hybridization. Loaded CPT release and cascade catalytic reactions are triggered by intracellular phosphate. TEM images of the PEG-Au/Fe-MOF@CPT NPs obtained using (d) 2.00×10^{-3} M PBS and (e) 10.00×10^{-3} M PBS. (f) Release profiles of CPT for different phosphate concentrations. Reproduced with permission.[79] Copyright 2020, Wiley-VCH.

Chen et al. reported PEG-modified nanoscale coordination polymers (NCPs) with the Ca^{2+}/dicarboxylic acid cisplatin (IV) prodrug for charge reversal, drug release, and subsequent internalization (**Figure 3a**).[75] To avoid the complexities involved in surface modification of PEG, a one-step procedure was developed to incorporate metal ions and organic ligands along with the poly-L-histidine-PEG copolymer in high yields. In a slightly acidic TME, imidazole groups in p-His underwent protonation with concomitant charge reversal to positive ions, leading to expansion and subsequently drug release (**Figure 3b**). An effective in vivo therapeutic outcome was achieved for solid tumors with reduced pH using a low cisplatin dose (3 mg kg^{-1}).

Focusing on the abundance of glutathione (GSH) in TMEs, Chen et al. designed an in situ polymerization strategy using PCN-224 (PCN: porous coordination network), ZIF-8, and

UiO-66 anchored to the bis[2-(methacryloyloxy)ethyl] phosphate (BMAP) ligand for stimuli-responsive drug release.[76] Various monomers such as cystamine, acrylic acid, PEGMA, and fluorescein dimethacrylate were polymerized on the MOF surface and conjugated with a variety of drugs. In situ polymerization resulted in enhanced physiological stability, thereby prolonging the in vivo circulation and enabling intracellular release of the drug. Controlled release using MOF–polymer hybrids has also been applied for other diseases such as glaucoma. Silvestre-Albero et al. developed a UiO-67-based polyurethane film for brimonidine tartrate (an ocular drug).[77] The composite was 60-times more effective than the polyurethane (PU) matrix in absorbing the drug, resulting in prolonged release in the liquid phase.

Polymer coating has also been performed to impart physiological stability in vivo and prevent catalytic activities arising from unintended interactions while in circulation.[78] Wang et al. fabricated gold-nanoparticle-decorated MOFs with cascade catalytic capability for camptothecin (CPT) release.[79] The porous structure of the MOFs was exploited to encapsulate the hydrophobic drug, and the surface-attached Au nanoparticles were modified with 1-dodecanethiol and methoxy polyethylene glycol thiol (PEG-SH) to impart stability and inhibit catalysis during circulation (**Figure 3c**). A CPT loading of 7.7% was achieved owing to π–π interactions and the coordination between Zr and the quinine group of CPT. At reduced pH, the carboxylate groups of TCPP(Fe) and quinine moiety of CPT were protonated, resulting in the dissociation of the MOFs and release of CPT **(Figure 3d–f**). The synergetic action of the catalytic reactions generated cytotoxic •OH and enabled glucose-based starvation therapy and pH-responsive drug release, inhibiting 85.6% tumor volume in vivo. In another study, Chen et al. designed gold-NP-anchored porphyrin MOFs encapsulated with DOX to target tumor hypoxia. The gold NPs served as radiosensitizers for boosting the chemoradiotherapy, and the attached PEG chains enhanced the stability and prevented phosphate-mediated premature degradation under physiological conditions.[80]

In a noteworthy study, Liu et al. prepared size-controlled DOX@AZIF-8 nanoparticles for pH-stimulated release of DOX.[81] The degree of supersaturation was controlled using water-soluble cationic poly(allylamine hydrochloride) (PAH) as a biocompatible capping agent. PAH functioned via competitive binding to Zn^{2+}, impeding the coordinative interactions between organic linkers and metal ions. Fine-tuned nanostructures ranging in size from 30, 40, 60, 90, 120 to 130 nm were prepared. Optimal tumor uptake and in vivo efficacy was achieved using the 60-nm-sized DOX@AZIF-8 nanosystem.

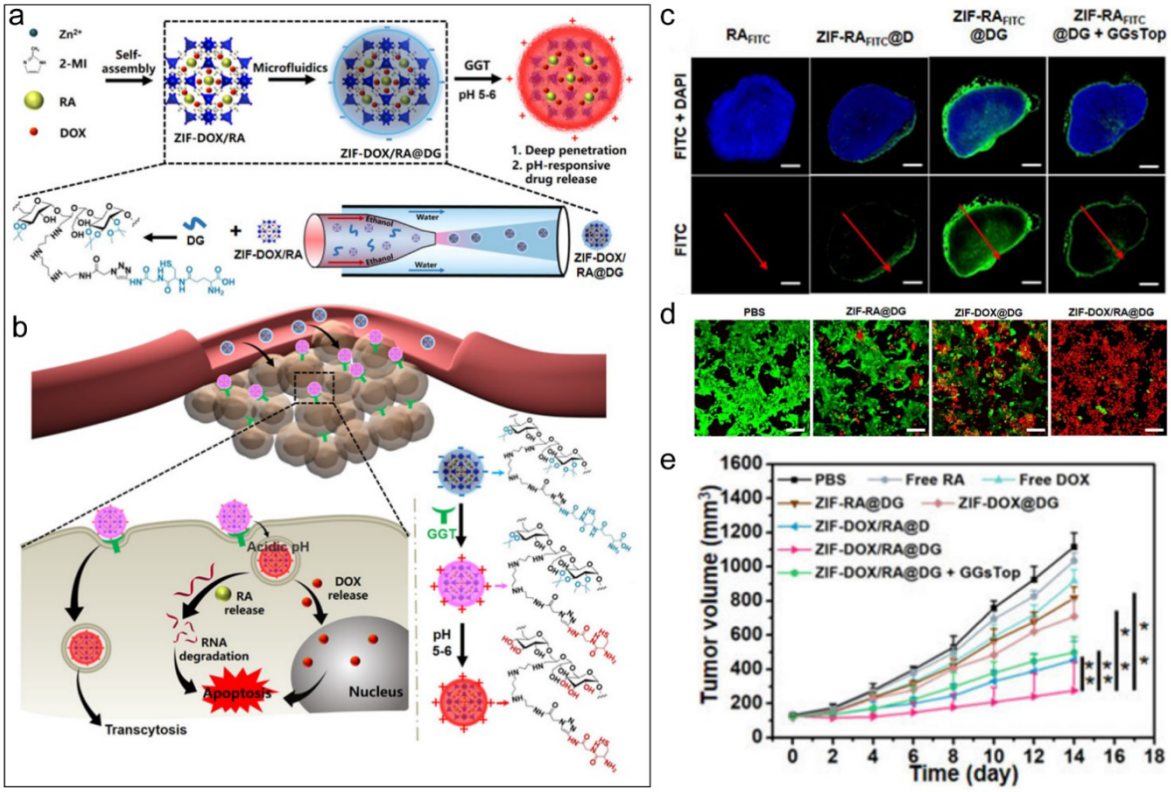

Figure 4. Investigation of ZIF-DOX/RA@DG for drug/protein codelivery. (a) Synthesis of DOX- and RA-loaded dextran-modified ZIF-DOX/RA@DG. (b) GGT-activable cationization and acidic-TME-triggered degradation. (c) Fluorescence distribution in PANC-1 tumor sections analyzed 4 h after administration for different groups in vivo (scale bars: 2 mm). (d) CLSM images showing live–dead staining of PANC-1 tumor cells undergoing various treatments and (e) tumor volumes of mice monitored for 14 days post-treatment with ZIF-DOX/RA@DG and other control groups (**p<0.01) (scale bars: 200 μm). Reproduced with permission.[84] Copyright 2022, Wiley-VCH.

Ryu et al. used hyaluronic acid (HA) as a gatekeeper on an enzyme-responsive HA-DOX-PCN-224 nanoMOF.[82] HA was selected as a biocompatible moiety owing to multiple factors such as its role in enabling coordinative interactions between the Zr cluster and COOH functional groups, and its ability to target CD44-overexpression, which impart stability and gatekeeping attributes. DOX molecules were released following the degradation of the HA coating by HAdase. In another study, HA-mediated CD44-overexpressed tumor recognition was analyzed using MIL-100/MTO/HA nanoparticles co-loaded with mitoxantrone (MTO) and an anti-OX40 antibody (αOX40).[83] The combined abscopal effect of MTO and αOX40 was realized by reversing immunosuppressive M2 macrophages and Treg cells in the TME.

In addition to small-molecule-based chemotherapeutic delivery, protein drug delivery using MOFs has been extensively probed. The rapid clearance of proteins after systemic administration, owing to their inherent properties, diminishes therapeutic efficacies. Proteins are frequently combined with small molecules for combination cancer therapy. However, co-loading and co-delivery of the two entities, which have substantially varied physicochemical properties, impede the development of single drug-delivery systems. To address these shortcomings, Chen at al. developed ZIF-DOX/RA@DG nanoparticles for dual-responsive co-release of ribonuclease A (RA) protein and DOX (**Figure 4a**).[84] ZIF-8 was coated with a dextran-based polymer network using a microfluidic approach. Dextran played a critical role in the transcytosis mediated by the absorption of gamma-glutamyl transpeptidase (GGT), with concomitant charge reversal to positive ions in a slightly acidic TME, resulting in enhanced tumor penetration and accumulation (**Figure 4b-d**). Moreover, the pH-responsiveness of dextran helped prevent premature drug release during circulation. Owing to the charge-reversal-mediated co-delivery of RA and DOX, synergetic tumor growth was inhibited to 77.9% (**Figure 4e**). Overall, these studies highlight the potential of stimuli-responsive-controlled drug-releasing MOF nanoparticles for clinical translation.

4.1.2. Photothermal Therapy. Photothermal therapy (PTT) is a light-based therapy that primarily involves the absorption of incoming light (photons) by photo-absorbing agents to convert the absorbed light to heat.[85] The photonic vibrational energy converted to heat increases the local temperature of irradiated cells to ~42–45 °C for ablating cancer cells in the vicinity.[86] Thus, PTT is a localized therapy independent of oxygen reliability and is capable of sensitizing tumor tissues to radiation or chemotherapy treatment. Advantages such as relatively simple operation, fast recovery, and short hospital stay have inspired the use of radiofrequency pulses, microwave radiation, and ultrasound waves as energy sources in clinical settings.[87] Parameters such as light absorptivity and photothermal conversion efficiency (PTCE) are optimized when designing novel photothermal agents (PTAs).

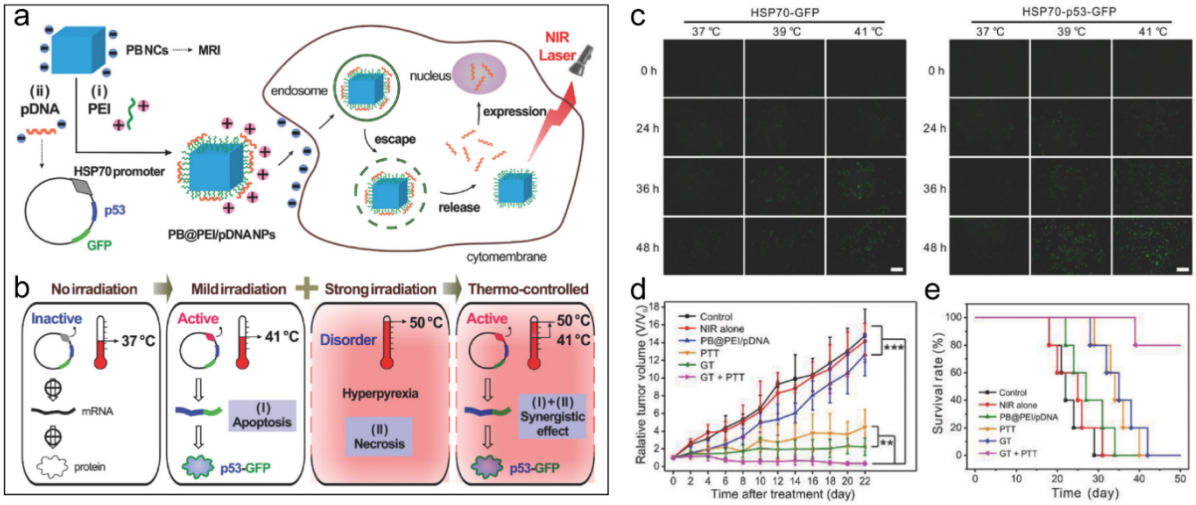

Figure 5. Preparation of PB@PEI/pDNA for thermo-controlled PTT. (a) Schematic illustrating the design of PB@PEI/pDNA NPs as PEI-modified PB nanocubes endowed with the HSP70 promoter for combined transgene expression and PTT. (b) Graphic describing the GT/PTT synergetic effect induced by thermo-controlled irradiation. (c) GFP expression of HSP70-GFP and HSP70-p53-GFP under mild near-infrared (NIR) activation (scale bars: 100 μm). (d) Relative tumor volume curves and (e) survival rates of HeLa-tumor-bearing mice injected with PB@PEI/pDNA nanoparticles (**p<0.01; ***p<0.001). Reproduced with permission.[90] Copyright 2018, Wiley-VCH.

Prussian blue (PB) is one of the oldest conventional photothermal-radiation-absorbing nanoMOFs. It is an FDA-approved therapeutic agent that is used to treat radioactive exposure. Charge transfer between Fe species with different oxidation states generates heat under NIR laser irradiation, emphasizing the potential of PB as an effective PTA. Yue et al. prepared differently sized (10–50 nm) citric-acid-capped PB from a solution of $FeCl_3$ and $K_4[Fe(CN)_6]$.[88] With a molar extinction coefficient of 1.09×10^9 M^{-1} cm^{-1} and 808 nm laser irradiation for 10 mins, the HeLa cell viability was reduced to less than 10%. Near-edge infrared absorbance (712 nm) and the seemingly low PTCE at 808 nm have inspired new strategies for coupling with PTT. Nanosystems with high PTCEs, circulation time, and tumor uptake were initially targeted. Subsequently, PTT agents combined with other therapeutic modalities were focused on. Image-guided PTT with multifunctional materials was explored thereafter for selective and targeted PTA delivery to the tumor location. Doping PB with metal ions such as Mn^{2+}, Zn^{2+}, Cu^{2+}, and Gd^{2+} at its interstitial or lattice sites helps tune its photothermal behavior by changing the electron density and orbital energy. PB has been doped with Mn^{2+} by replacing $FeCl_3$ with $MnCl_2$ in the synthesis protocol and further coated with

PAH, PAA, and PEG using layer-by-layer technology.[89] Increased red-shifted absorption with enhanced r_1 relaxivity and biocompatibility have enabled in vivo MRI and photoacoustic-imaging (PAI)-guided PTT.

Employing an innovative approach to hasten PTT-induced death, Chang et al. devised PB@PEI/HSP70-p53-GFP (HSP70: heat shock protein 70; GFP: green fluorescent protein) for gene-therapy (GT)-aided PTT.[90] Here, therapeutic DNA (HSP-p53-GFP) was loaded onto polyethyleneimine-modified PB through electrostatic interactions (**Figure 5a**). Under mild NIR-laser irradiation (41 °C), the heat shock effect of the HSP70 promoter triggered GFP expression, which was correlated with transfected HeLa cells for elevated p53-expression-mediated apoptosis (**Figure 5b**). Moreover, strong near-infrared (NIR) laser irradiation (50 °C) led to cellular dysregulation and necrosis (**Figure 5c**). The strong-NIR-laser group with combined GT and PTT regressed tumor growth in vivo for up to 22 days, prolonging the lifetime of mice (**Figure 5d,e**).

Compared to inorganic gold nanostructures, carbon-based structures, and organic dyes, photo-absorbing polymers—such as PANI[91], polypyrrole (PPy)[92], PDA,[93,94] and other conducting polymers[95]—exhibit remarkable absorptivity and photostability. Xie et al. prepared water-dispersible hybrid UiO-66@PAN nanoparticles for PTT-mediated cancer ablation.[96] The positively charged NIR-absorbing polymer PANI was adsorbed via in situ polymerization onto negatively charged UiO-66 through electrostatic interactions. With a calculated PTCE of 21.6%, 93% tumor volume was suppressed in vivo under 808 nm laser irradiation. Wang et al. self-polymerized dopamine into the MnCo skeleton through π–π interactions (**Figure 6a**).[94] To improve the stability, biocompatibility, and tumor accumulation, cyclic PEG- and thiol-terminated arginine/glycine/aspartic-acid peptides were loaded to yield MCP-PEG-RGD (RGD: arginyl-glycyl-aspartic acid) (**Figure 6b,c**). The high PTCE (41.3%) was attributed to the enhanced electron density in the complex nanosystem (**Figure 6d,e**). Owing to a tumor accumulation of 8.3% injected dose (ID) and the enhanced inhibitory rate of tumors in vivo, the MOF–polymer nanogels served as MRI and fluorescence-guided multiplex theranostic agents (**Figure 6f,g**).

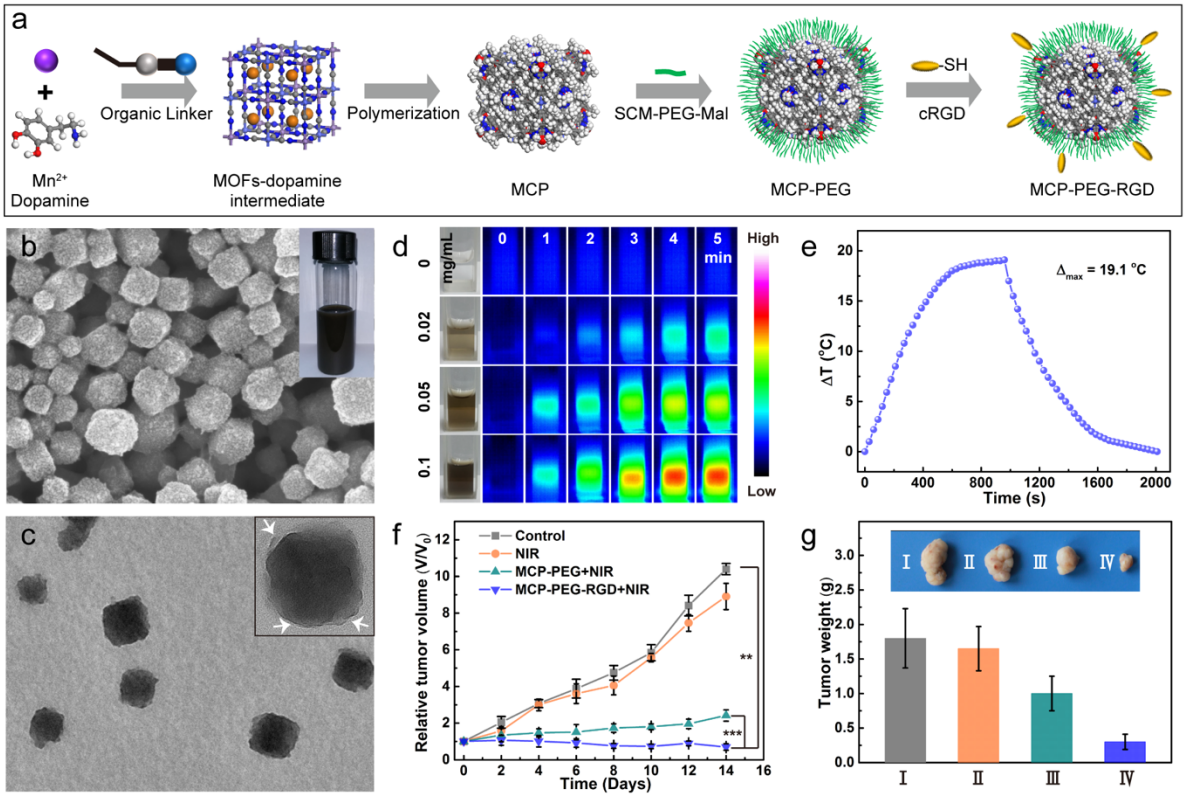

Figure 6. Schematic illustration of the MCP-PEG-RGD system used for PTT. (a) Stepwise development and surface modification of PEG-coated MCP NPs. (b) SEM image of MCP, and (c) TEM image of MCP-PEG. (d) Thermal images obtained using different MCP concentrations under 808 nm laser irradiation (1 W cm^{-2}) for 5 min. (e) Temporal variation in temperature for the 0.05 mg mL^{-1} specimen. (f,g) In vivo tumor volumes and weights of different groups for HeLa-tumor-bearing mice (**p<0.01; ***p<0.001). Reproduced with permission.[94] Copyright 2018, Wiley-VCH.

Pang et al. coated PPy onto an Fe-soc-PEG-modified MOF (the isostructural analog of In-soc-MOF) to develop a multifunctional theranostic platform.[97] Owing to the presence of Fe nodes, the nanocomposite was used for T_2-weighted MRI. The small amounts of PPy that covered the surface of Fe-soc-MOF (15 wt%; TGA) were responsible for the low PTCE (13.9%). Despite the low PTCE, the system exhibited considerable tumor inhibition. A slightly enhanced PTCE (27.3%) was obtained for PPy@MIL-53.[98] The MIL-53 minireactor provided Fe ions with unsaturated coordination sites to oxidize Py to PPy. Under 808 nm laser irradiation for 5 min, more than 90% of the 4T1 cells were made vulnerable to ablation. Owing to the pH- and NIR-controllable drug release, the in vivo tumor weights decreased several folds for the treatment group.

In another study, core–shell PPy@MIL-100(Fe) nanocomposites were synthesized for MRI/PA-guided synergistic chemo-photothermal therapy.[99,100] Initially, Fe^{3+}-doped PPy nanoparticles were prepared using PVP as the stabilizer. Subsequently, MIL-100(Fe) was grown on the surface of the PPy nanoparticles with trimesic acid utilizing Fe(III) as reactive sites. A considerably enhanced PTCE of 40% led to a cancer cell eradication of 90% in vitro, with the synergistic release of DOX. MRI and PAI revealed concentration-dependent behavior. Hence, in situ polymerization can enhance the therapeutic efficacy of nanoMOFs.

To augment the intrinsic PTT abilities of the prepared MOFs, PTAs such as IR825, perylenediimide, and ferrocene have been employed during synthesis.[101,102] The gradual decomposition of NMOPs in the presence of phosphate or water molecules in body fluids via ligand-exchange reactions is the major advantage of these systems. In an interesting study, Fan et al. employed the COOH groups of cyanine dye to coordinatively interact with Cu^{2+} ions having a surface coating of HA to form HA@Cy-Cu nanoparticles for CD44-receptor-mediated targeting.[103] The prepared system achieved a PTCE of 42.3%. Through reduction to Cu^{+}, Cu^{2+} served as a chemodynamic agent by down-regulating GSH and helped up-regulate the •OH-mediated oxidative damage. The HA@Cy-Cu + light group showed complete tumor inhibition at a low dose of 5 mg kg^{-1} and under the combined effect of PTT and chemodynamic therapy (CDT). Liu et al. fabricated 1D-NCPs through the self-assembly of Mn^{2+} and indocyanine green (ICG) using a phase-transfer strategy.[104] The 1D-NCPs were then PEGylated and loaded with gambogic acid (GA) as an HSP90 inhibitor to facilitate low-temperature apoptotic PTT. A peptide-containing imidazole side chain, poly-histidine, underwent charge conversion from neutral to positive through protonation at pKa = ~6.0, thus improving the solid-tumor-targeting efficiency and specificity. After low-temperature (43 °C) PTT using Mn-ICG@pHis-PEG/GA, the proportion of early and late apoptosis was found to be 54% and 23.2% respectively, which were higher than those of the other groups.

4.1.3. Photodynamic Therapy. Photodynamic therapy (PDT) is another light-based therapy that essentially involves exciting a photosensitizer in the singlet ground state to the triplet state under visible or NIR light irradiation.[105] Two probable photochemical reaction pathways (Types I and II) may advance PDT. In Type-I PDT systems such as fullerenes, the activated triplet-state photo-absorber reacts with biological tissue to produce radicals, which further react with $^3O_2$ or H_2O to yield hydroxyl (•OH) or superoxide (O_2•$^-$) radicals. In Type-II PDT systems such as the organic photosensitizer chlorin e6 (Ce6), the activated triplet-state photo-absorber transfers energy to $^3O_2$, thereby generating cytotoxic $^1O_2$.[106] Elaborate PDT-based strategies

are being adopted to successfully develop photo-agents that could cure advanced cancers. The most common strategy involves optimizing the properties of the target TME, which is characterized by hypoxia, overexpressed GSH, acidity, and presence of adenosine-5'-triphosphate (ATP). Because PDT relies heavily on the local oxygen concentration, its efficacy is highly impaired in the hypoxic TMEs. Moreover, GSH is a natural antioxidant present in the body to safeguard against the deleterious effects of ROS, which further diminishes the PDT efficacy.

Considering the aforementioned aspects, we developed a PB analog self-assembled from metal ions, photosensitizers, and organic bridging ligands with PVP protection to form a $Mn_3[Fe(CN)_6]_2$-Ce6 photodynamic nanoagent,[107] which exhibited pH-responsive dual action in an acidic TME. In its operational mechanism, Ce6 molecules are initially released to potentiate ROS generation upon laser irradiation. Subsequently, $[Fe^{III}(CN)_6]$ is reduced to $[Fe^{II}(CN)_6]$, followed by GSH depletion. As the tumor sizes were reduced by several folds in vivo, this study demonstrated ROS-amplified and GSH-depleted synergetic tumor therapy. MOF-based single-atom enzymes (SAEs) have been prepared in an interesting approach to enhance the PDT effect in hypoxic tumors.[57] With $Mn_3[Co(CN)_6]_2$ as the support, Ru single-atoms were incorporated for endogenous oxygen generation. OxgeMCC-r SAE was self-assembled via multi-coordination-driven interactions from the bonding linkers, metal ions, and photosensitizers in the presence of PVP (**Figure 7a**). OxgeMCC-r assisted in delivering Ce6, resulting in 95% cancer ablation (**Figure 7b,c**). The remarkable PDT efficacy was attributed to the oxygen supply generated by single-atom catalysis in the presence of over-expressed H_2O_2. The tumor volumes were drastically reduced compared to other groups with similar dosages (**Figure 7d**). Immunofluorescent staining corroborated the alleviation in hypoxic tumor conditions. Furthermore, the Mn nodes were targeted in the MRI to monitor the accumulation of the nanoagent in the tumor region, optimize the laser treatment time, and track the impact of the treatment (**Figure 7e**).

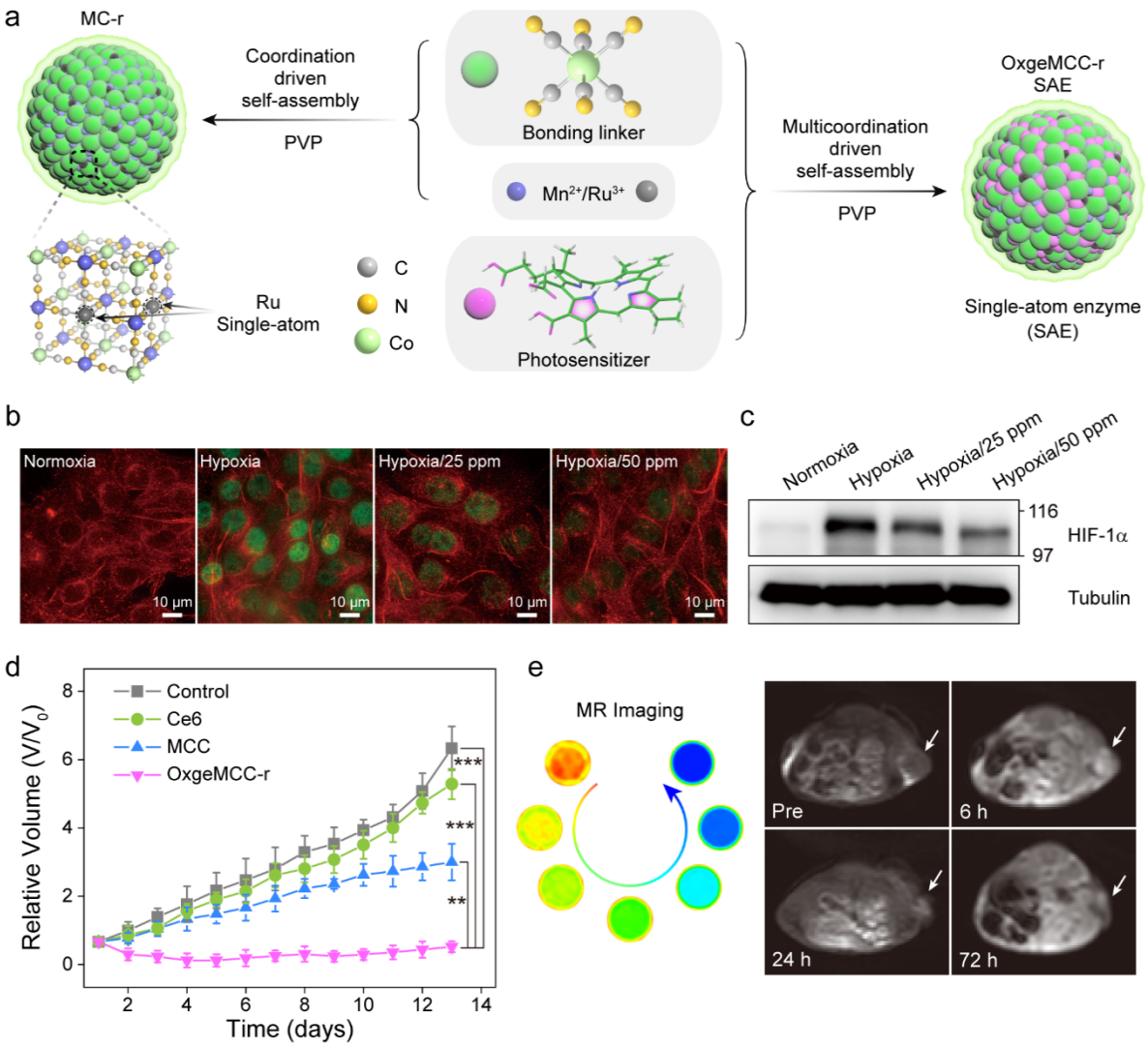

Figure 7. Investigation of OxgeMCC-r for enhanced PDT. (a) Design of the OxgeMCC-r SAE with a Ru single-atom and PVP-protected layer. (b) Fluorescence images of HIF-1α (green)- and tubulin (red)-stained 4T1 cells for different concentrations of MC-r under normoxic and hypoxic conditions, and (c) the corresponding western blot expression. (d) In vivo tumor volumes, and (e) in vitro and in vivo images of 4T1-tumor-bearing mice undergoing a variety of treatments. (**p<0.01; ***p<0.001) Reproduced with permission.[57] Copyright 2020, Springer Nature.

Zhang et al. developed a core–shell-type nanostructured $MnFe_2O_4$@MOF to achieve persistent oxygen generation and a reaction with GSH for realizing catalase- and peroxidase-like activities, respectively.[108] The MOF was subsequently coated with PDA and PEG to enhance biocompatibility and photoactivity. A continuous catalytic reaction cycle was created when both Fe^{2+} and Mn^{2+} transformed into their oxidized forms (Fe^{3+} and Mn^{4+}) through

a Fenton reaction and reverted to their reduced forms after reacting with GSH and H_2O_2. The $^1O_2$ generation of $MnFe_2O_4$@MOF under hypoxic conditions was improved because of the O_2 supply. In the presence of GSH and after 3 min of irradiation, only 17.6% of the $^1O_2$ generated by $MnFe_2O_4$@MOF was depleted by GSH compared to that of Zr-TCPP (57.4%).

Porous organic polymers (POPs) comprise periodically arranged organic building blocks. Similar arrangements of photoactive molecules can help optimize the intermolecular distance with refined molecular vibration, preventing aggregation-induced quenching. POPs are advantageous because of their tunable particle size and shape. Among the efforts devoted to controlling the morphology and size of POPs, the template strategy is particularly beneficial for preparing MOF–POP hybrid nanostructures, with the MOFs containing cavities and surface defects acting as excellent templates.

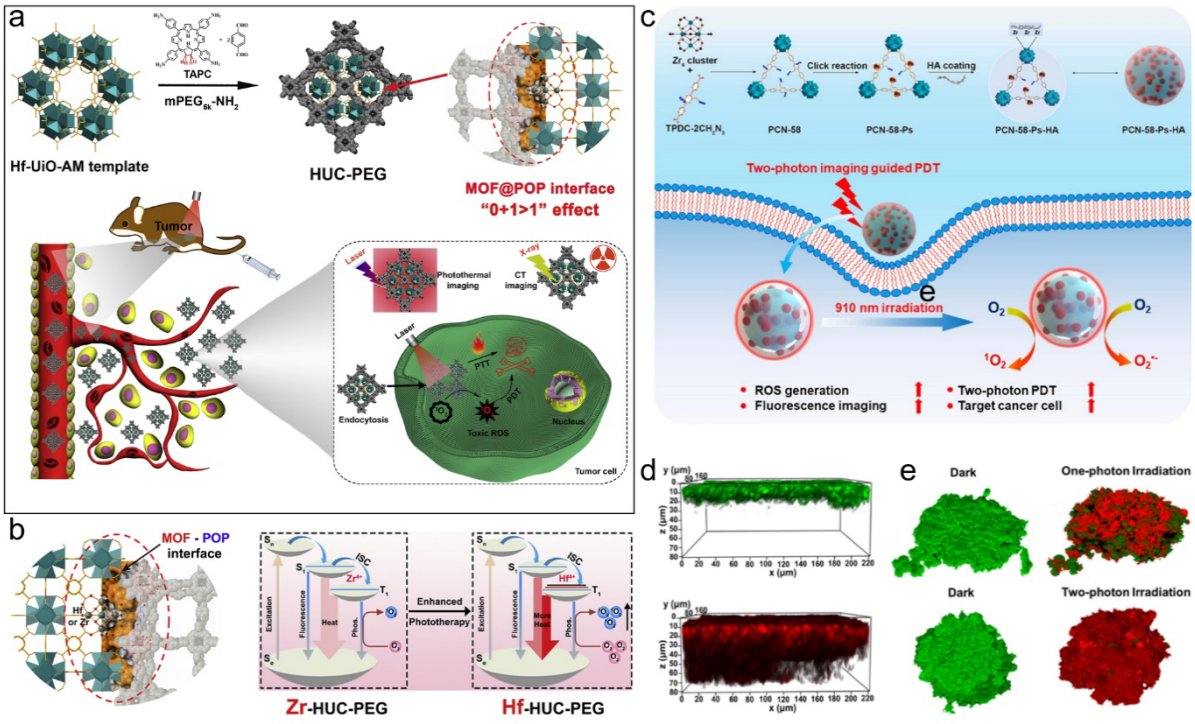

Figure 8. Design and synthesis of HUC-PEG and PCN-58-Ps-HA for improved PDT. (a) Development of a CT-imaging-enabled theranostic platform using the MOF@POP interface. (b) Pictorial representation of the mechanism underlying the '0+1>1' amplification effect with boosted phototherapy. Reproduced with permission.[109] Copyright 2020, Elsevier. (c) Schematic showing the preparation of light-induced ROS production and two-photon imaging-directed PDT. 3D fluorescence images of HeLa (d) tumor tissues and (e) multicellular tumor spheroids stained with Syto 63 (green, living cells) and PI (red, dead cells) acquired before and after one-photon (561 nm, 0.2 W cm^{-2}) and two-photon (910 nm, 0.2 W cm^{-2})

irradiation, respectively. Reproduced with permission.[114] Copyright 2021, American Chemical Society.

Xie et al. developed an MOF@covalent-organic-framework (COF) system using tetrakis(4-aminophenyl)-21H-23H-chlorin (TAPC), terephthaldehyde, and PEG-HN_2 as the COF sources and Hf-UiO-66 as the MOF source (**Figure 8a**).[109] PEG was used to impart physiological stability and intratumoral accumulation. A tumor inhibition rate of 88.4% was achieved in vivo under 671 nm light irradiation, which was attributed to the synergistic effect of PTT and PDT. The anticancer mechanism was correlated by comparing the half-maximal inhibitory concentration (IC_{50}) values under different therapeutic conditions. The IC_{50} of combined PDT/PTT (73.6 μg mL^{-1}) was significantly lower than those of plain PDT (315.5 μg mL^{-1}) and PTT mixed with vitamin C (104.3 μg mL^{-1}). The interfacial synergy derived from the Hf heavy element between the UiO-AM and TAPC was responsible for enhancing the performance of PDT and PTT (**Figure 8b**).

As mentioned previously, the photosensitizers operating through the Type-II PDT mechanism are limited by oxygen supply. In an alternative strategy, the •OH radicals generated in Type-I PDT can react with almost all biomolecules, consequently inducing more oxidative damage than that by $^1O_2$. Xie et al. constructed a POP by coating boron-dipyrromethene (BODIPY) onto the MOF surface as a template to generate an MOF@POP nanostructure.[110] The growth of the BODIPY-based POP was visible as purple coloration on pale-yellow MOFs. Because of pH responsiveness, potent cytotoxicity against cancer cells was achieved with an apoptotic rate of 64.7%, and toxic •OH was generated upon light irradiation. Therefore, the nanosystems prepared using intrinsic photoagents can help realize combined PDT/PTT for multifunctional applications.[111]

It is worth noting that conventional PDT, which involves PSs exhibiting activity in the wavelength range 650–800 nm, is effective for tissue depths of only 3–10 mm^2.[112] Thus, light of longer wavelength cannot excite PSs, despite achieving greater penetration.[105] Moreover, incident light of wavelength greater than 800 nm does not provide sufficient energy to react with $^3O_2$.[113] The limited tissue penetration of conventional PDT sensitizers inspired Li et al. to explore two-photon PDT, wherein two NIR photons are utilized for activation, resulting in higher spatial specificity and penetration depth.[114] A porous functional material, PCN-58-Ps-HA, was prepared using a click reaction and coordinative interactions (**Figure 8c**). The click reaction established a link between a PS in the D-π-A configuration and the Zr_6 cluster, and HA was coated thereafter to target tumors. Considerable two-photon activity and

ROS generation were observed under 910 nm laser excitation. The two-photon excitation reached a greater depth (80 μm) than that achieved by one-photon excitation (30 μm; 571 nm) (**Figure 8d,e**). In vivo experiments on this system could have helped in exploring the nonlinear optical behavior of the MOFs.

4.2. Biomedical Imaging. Bioimaging techniques such as MRI, PAI, fluorescence imaging (FLI), computed tomography (CT), and photothermal imaging (PTI) serve as diagnostic tools for noninvasive visualization and quantification of biological processes and diseased states. Imaging agents are organic or inorganic components comprising concentrated contrast moieties; moreover, they exhibit decent physiological stability and target enrichment characteristics. The use of MOF–polymer hybrids for biomedical imaging adds multidirectional functionality to imaging capabilities. Biologically relevant MOFs with various metal nodes exhibiting attractive properties such as straightforward preparation, surface functionalization, aqueous stability, and high surface area are potent candidates for exhibiting intriguing optical and magnetic characteristics. Additionally, polymers exhibit characteristics such as biocompatibility and occasional inherent imaging capabilities. Consequently, MOF–polymer hybrids are an appealing choice for preclinical and translational research. In the following section, various studies on the utilization of MOF–polymer hybrids for monomodal and multimodal bioimaging are discussed.

MRI, which utilizes interactions between an external magnetic field and a subject, has rapidly become a staple within the diagnostics field since its inception in the 1970s. In MRI, both T_1 and T_2 relaxation (also expressed as r_1 and r_2 relaxivity, respectively) are modulated to obtain sensitive contrast images. Wang et al. prepared a PEG-protected copper hexacyanoferrate (Cu-HCF) single-site nanozyme for tumor therapy and MRI.[115] The outstanding feature of this study was the incorporation of an appropriate amount of Cu single-atoms (21.4%; **Figure 9a**). The high-spin species Cu-N_6 (S = 1/2) imparted in vivo magnetic-resonance-tracking capabilities (**Figure 9b,c**). Wang et al. prepared a multifunctional mesoporous nanozyme comprising MOF-derived manganese-cobalt-oxide NPs that was further coated with PDA and PEG.[116] Apart from being a good candidate for antitumor therapy, with features such as decomposition of H_2O_2 into O_2 in PDT, the system served as a T_2-weighted MRI contrast agent owing to the presence of metal ions. The T_2 transverse relaxation resulted in increasing dark contrast with circulation time up to 24 h for indicating tumor accumulation.

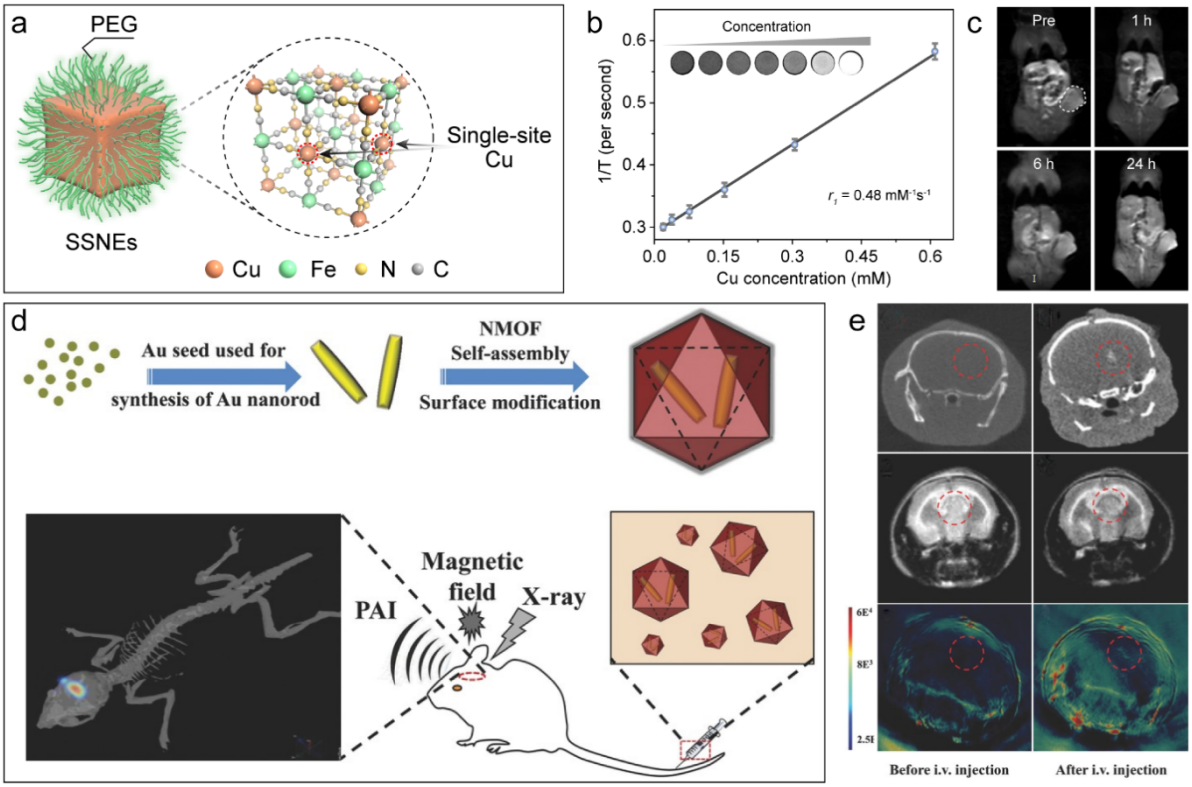

Figure 9. Pictorial representation of SSNEs and Au@MIL-88(Fe) developed for biomedical imaging. (a) Schematic of PEG-protected Cu-HCF developed for tumor therapy mediated by an SSNE-based cascade enzymatic reaction. The highlighted Cu active-sites are octahedrally coordinated to $[Fe^{II}(CN)_6]$ via N terminals. (b) Plot constructed to determine the longitudinal relaxivity of Cu, and the (c) T_1-weighted MRI contrast ability in 4T1-bearing mice at the preceding, 1 h, 6 h, and 24 h stages. Reproduced with permission.[115] Copyright 2020, Wiley-VCH. (d) Schematic of the Au@MIL-88(Fe) system capable of multimodal-imaging-based tumor diagnosis. (e) High-depth, high-sensitivity imaging of U87 MG-orthotopic tumor mice via CT, MRI, and PA before and after intravenous injection of Au@MIL-88(Fe). Reproduced with permission. [119] Copyright 2017, Wiley-VCH.

Despite its astounding features, MRI suffers from limited spatial resolution and is unsuitable as a monomodal imaging guide. Thus, MRI must be combined with other imaging techniques such as FLI, CT, and PAI.[117,118] With a focus on early and integrated diagnosis of gliomas, which can prevent high fatality rates, Shang et al. synthesized core–shell nanoparticles of Au@MIL-88(Fe) using the microemulsion process (**Figure 9d**).[119] Au nanorods provided CT enhancement and PAI optical signals, whereas the NMOF shells contributed to T_2-weighted MRI. To prevent the in vivo clotting and aggregation of the nanoparticles, the surface was modified with PEG-COOH to form a superficial PEG 'brush.' Extensive in vitro imaging

experiments established a direct linear relationship between the probe concentration and signal contrast. Moreover, in vivo studies on mice bearing a U87 MG subcutaneous tumor demonstrated remarkable efficiency (**Figure 9e**). CT signals at 8 h post-injection indicated accumulation within the tumor site. Similarly, the T_2-weighted MRI signals showed a darkening effect after 12 h, suggesting high passive tumor uptake. The PAI signals also showed enhanced signals. These results collectively demonstrate the effectiveness of the prepared Au@MIL-88(A) hybrid in achieving triple-modal imaging modalities for orthotopic deep gliomas with high contrast, penetration depth, and spatial resolution.

4.3. Biomedical Sensing. Advances in biosensing technologies can facilitate early detection of substantial changes in organisms and monitoring of metabolic processes. The dangling bonds present on the linkers of MOFs serve as anchors for hydrogen bonding with an analyte for electrocatalytic reduction/oxidation, whereas the π–π interactions between the aromatic units of the analyte and conducting polymers aid in selectively detecting analytes. Consequently, MOF–polymer nanohybrids exhibit unique advantages such as an abundant surface area for efficient immobilization of biomolecules and diffusion of analyte molecules. The readily tunable hydrophobic properties of polymers could enhance the stability and reactivity of MOFs toward immobilized enzymes. Additionally, the introduction of polymers into MOFs can improve electrode conductivity by facilitating electrocatalytic site generation, thereby enhancing sensitivity and response times.

For sensing-related applications, analyte-induced changes can be monitored using various phenomena such as electric potential generation, luminescence, absorption, and fluorescence. Attributes such as selectivity, reproducibility, stability, and applicability are crucial in developing sensors for analyte detection to ensure their post-fabrication use. Typically, three electrochemical techniques are used to study the preparation, characterization, and application of sensors: (1) cyclic voltammetry (CV), differential pulse voltammetry (DPV), and electrochemical impedance spectroscopy (EIS). In the following section, MOF–polymer-based sensors developed to detect small molecules, biomacromolecules, pathogens, and immunosensors are highlighted. Highly adjustable channel structures and controllable pore sizes have driven chemical-sensing research toward physiologically relevant guest molecules, such as glucose, dopamine, hydrogen peroxide, and amino acids, for encapsulation.

4.3.1. Glucose Sensing: Accurate real-time sensing of glucose is crucial for diagnosing diabetes mellitus, which is associated with a myriad of cardiovascular diseases. Electrochemical biosensors based on GOx, an enzyme that catalyzes the oxidation of glucose to hydrogen peroxide and gluconolactone, are typically employed to detect glucose. Li et al. prepared a magnetic Fe_3O_4/PPy@ZIF-8 nanocomposite for electro-detection of glucose (**Figure 10a**).[120] Polymerization of PPy onto Fe_3O_4 helped impart electrical conductivity and antifouling properties (**Figure 10b**), whereas in situ growth of the MOF assisted in creating a medium to immobilize the enzyme components and making the nanocomposite more stable. The as-prepared amperometric biosensor showed activity over a wide range of glucose concentrations (1 μM to 2 mM) with a detection limit of 0.333 μM.

4.3.2. Dopamine Sensing: Dopamine is a neurotransmitter that is responsible for transmitting impulse signals between neurons in the central nervous system of mammals. Accurate dopamine detection is critical in diagnosing and treating several neurological disorders, such as dependency syndrome and schizophrenia, and other cognitive issues such as the involuntary tremors caused by Parkinson's disease. Wang et al. prepared a glassy carbon electrode (GCE) coated with a Nafion/polyaniline/ZIF-8 nanocomposite for dopamine determination.[121] The nanocomposite exhibited remarkable catalytic performance in PBS primarily owing to the synergetic effects of the conducting PANI and ZIF-8, with the detection limit as low as 1.2×10^{-8} mol L^{-1}. Subsequently, Jie et al. prepared an MOF based on a Cu-tetrakis (4-carboxyphenol) porphyrin and decorated it with conductive poly(xanthurenic acid) p(XA) and gold nanoparticles to develop an electrochemical ratiometric dopamine sensor, with paracetamol as the reference (**Figure 10c**).[122] The prepared PXa/Au/Cu-TCPP/GCE electrode exhibited a detection limit of 1.0 μM, which was comparable to that of other carbon-based electrodes.[123]

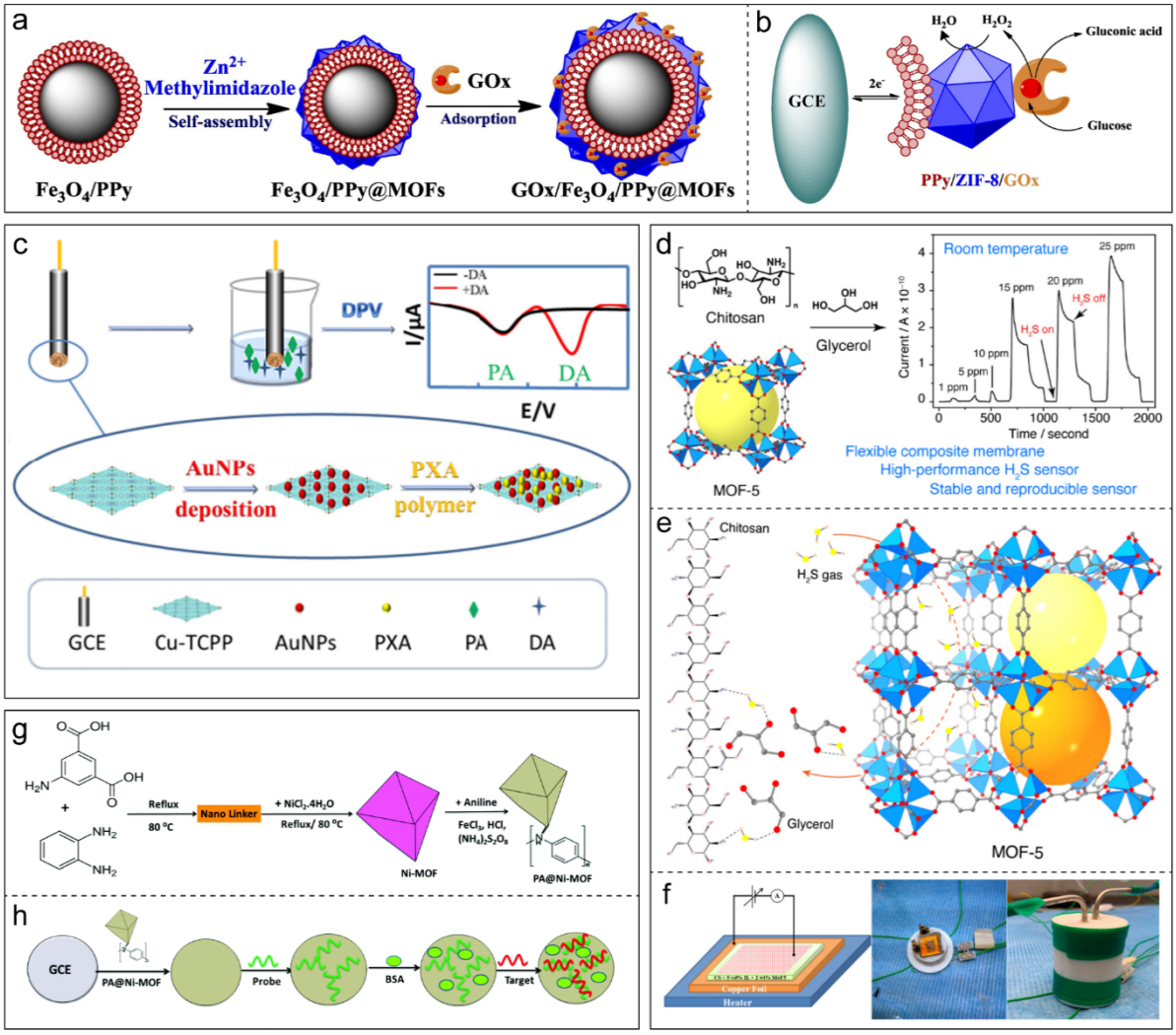

Figure 10. Design and operation of $GO_xFe_3O_4$/PPy@ZIF-8, p(XA)/Au/Cu-TCPP/GCE, MOF-5/CS/IL, and PA@Ni-MOF systems for biomedical sensing. (a,b) Synthesis strategy and glucose-detecting mechanism of the Fe_3O_4/PPy@ZIF-8 composite. Reproduced with permission.[120] Copyright 2018, Elsevier. (c) Schematic of ratiometric dopamine-detecting p(XA)/Au/Cu-TCPP/GCE-based electrochemical sensor. Reproduced with permission.[122] Copyright 2019, Elsevier. (d) Schematic illustrating the preparation of MOF-5 and a chitosan-based polymer MMM, and electrical response of the MOF-5/CS/IL membrane for H_2S detection. (e) Proposed mechanism for gas sensing. The Zn, S, N, O, C, and H atoms on the polymer chain are shown in aqua, yellow, blue, red, grey, and pastel red, respectively. (f) Schematic and photographs of the sensor setup and sensitivity test chamber. Reproduced with permission.[126] Copyright 2021, American Chemical Society. (g) Chemical synthesis of PA@Ni-MOF via oxidative polymerization of aniline. (h) Schematic showing the preparation of the HCV/nucleic-acid biosensor. Reproduced with permission.[124] Copyright 2020, Royal Society of Chemistry.

4.3.3. Hydrogen Peroxide Sensing. As a principal member of ROS, hydrogen peroxide is a highly abundant yet harmful molecule in living systems. Abnormal concentrations of hydrogen peroxide lead to diseases such as Alzheimer's, Parkinson's, and cancer. Therefore, efficient and reliable methods are required to detect hydrogen peroxide. Park et al. prepared a UiO-66-NH_2@P(ANI-co-ANA) hybrid nanocomposite derived from a copolymer (grafted aniline and anthranilic acid) and an MOF (UiO-66-NH_2).[124] The conducting copolymer prepared using aniline and poly(anthranilic acid) exhibited efficient electron flow, thus improving the overall conductivity, whereas UiO-66-NH_2 served as a high-surface-area adsorbent. In a detection range of 25–500 μM, the nanocomposite detected H_2O_2 up to 0.6 μM with a sensitivity of 1396.1 μA μM^{-1} cm^{-2} by chronoamperometry, producing higher-intensity signals in the presence of interfering species. Additionally, the prepared system selectively detected dopamine with a detection limit of 0.3 μM. In another study, ATP molecules and Ce(III) ions were coordinated in tris-HCl buffer to prepare ATP-Ce-Tris coordination polymer nanoparticles for fluorescent sensing of H_2O_2 and glucose.[125] A detection limit that was two-orders-of-magnitude lower than that of other Ce-based sensors was achieved for H_2O_2 at 0.6 nM. Reversible switching between the Ce^{3+} and Ce^{4+} ions enabled antioxidant characteristics with visible fluorescence quenching at 350 nm at high H_2O_2 concentrations. The prepared ATP-Ce-Tris coordination polymer nanoparticles achieved linear glucose detection with a limit of 65 μM.

4.3.4. Sensing Other Molecules. Hydrogen sulfide (H_2S) is a highly corrosive, flammable, and toxic gas that deteriorates human health and the environment because of its heavier-than-air nature and settlement in enclosed spaces. Recently, Mahmoud et al. developed an H_2S sensor with 1 ppm sensitivity by embedding MOF-5 microparticles into a flexible chitosan-based MMM (**Figure 10d,f**).[126] The remarkable room-temperature sensitivity of the sensor resulted from the synergistic effect of proton transfer from the gas molecules to the abundant nonbonded electrons on the N and O atoms in chitosan chains and the Zn oxo clusters in the MOF (**Figure 10e**). Other analytes such as alcohols warrant accurate detection in environmental, health-associated, and food-related industrial processes. Sachdeva et al. incorporated varying amounts of NH_2-MIL-53(Al) into a Matrimid polymer matrix to detect methanol in the gaseous phase.[127] A 1.75-fold enhanced response time was achieved compared to that of pure Matrimid using 40 wt% MOF, which was attributed to the rigidification of the MOF–polymer interface.

Biological macromolecules with molecular mass greater than 1000 Da, such as nucleic acids (DNA and RNA) and proteins (enzymes), are crucial for normal physiological functions in living organisms. Because their anomalies could have a deleterious effect, accurate monitoring is essential for disease prognosis, diagnosis, and effective treatment. In this regard, Dionysiou et al. coated a Ni-MOF (Ni-MOF@polyaniline) with in situ polymerized polyaniline on a GCE to detect and quantify the ribonucleic acid of hepatitis C virus (HCV-RNA) (**Figure 10g**).[128] In the described direct-detection route, electrochemical readings that were measured as charge-transfer resistance, which originated from the interactions between the HCV probe and its target, directly correlated with the HCV target concentration (**Figure 10h**). The increased resistance to charge transfer indicated the formation of nucleic acid double strands between the target and probe, leading to a linear detection range of 1 fM to 100 nM and a detection limit of 0.75 fM for HCV nucleic acid. In recent years, molecularly imprinted polymers (MIPs) have been extensively developed to analyze and detect biomacromolecules.[129] MIPs possess complementary cavities that can bind to target biomolecules, much like the antigen–antibody binding in biological scenarios.[130] In an interesting study, Cai et al. developed fluorescence sensors based on MIPs and a luminescent MIL-101-NH_2 MOF to detect hepatitis A virus (HAV).[131] The biosensor detected HAV within the range 0.02–2.5 nM and exhibited a detection limit of 3 pM within 15 mins.

The analysis of biomarkers in blood helps identify diseased conditions at an early stage, emphasizing the significance of accurate sensing and detection. Cardiac troponin I (cTnI) and GL-3 are protein biomarkers found in the bloodstream. They can help assess the cardiovascular risk in scenarios involving heart muscle damage. Deep et al. developed an impedimetric sensor based on a Cu-MOF composite ($Cu_3(BTC)_2$/PANI) using $Cu_3(BTC)_2$ and carboxylic-acid-functionalized PANI, and further immobilized it with anti-cTnI antibodies.[132] Upon mixing the bare MOF and PANI, the obtained $Cu_3(BTC)_2$/PANI electrode showed significant attenuation in the overall resistance compared to that of the $Cu_3(BTC)_2$ electrode. The cTnI antigen was detected over the dynamic concentration range 1–400 ng mL^{-1} with a detection limit of 0.8 ng mL^{-1}. Atar et al. prepared an amperometric immunosensor for GL-3 detection in plasma using gold-nanoparticle-functionalized graphitic carbon nitride (g-C_3N_4@Au) and a Ti-based MOF@COF.[133] The immunosensor achieved highly sensitive GL-3 detection at extremely low concentrations (0.025 pg mL^{-1}). This was due to the enhanced penetration of anti-GL-3-Ab_2 into the pore channels created in the MOF@COF

composite for facilitating stronger electrostatic/hydrogen-bonding and stable antigen–antibody interactions.

4.4. Antibacterial Strategies. With the rise in pathogenic-bacteria-induced infectious diseases, such as sepsis, respiratory inflammation, and dermatitis, novel antibacterial approaches are being actively pursued to alleviate public concerns. This is particularly crucial for addressing the adaptive drug resistance of pathogens that is plaguing conventional antibiotics and therapeutic systems. Nanotherapeutics-based antibacterial strategies have shown promise in this regard. Owing to their inherent antibacterial properties, nanosystems such as silver nanoparticles,[134,135] zinc oxide,[136,137] and carbon-based nanomaterials[138] have been used as alternative antimicrobial agents. However, these nanomaterials have inherent drawbacks and cannot be used repeatedly.[139] As a new class of anti-bacterial agents, MOF–polymer systems offer certain advantages: 1) Several metallic centers of MOFs, such as Ag, Cu, Ni, and Zn, exhibit bactericidal effects.[140] 2) The highly adjustable pore sizes of MOF–polymer systems could encapsulate antimicrobial agents of different molecular weights. 3) Porphyrin-based organic linkers could be used to activate PDT, thereby ablating bacterial cells via ROS generation. 4) The straightforward post-modification could help anchor functional polymers for added therapeutic handles.

Fan et al. fabricated a graphene-integrated ZIF-8 MOF for localized bacterial eradication with phase-to-size transformation.[141] An oxygen-rich graphene oxide surface was used to coordinate with Zn^{2+} via electrostatic interactions, and 2-methylimidazole was further added to yield a nanorhombic dodecahedron ZIF-8@GO (**Figure 11a**). Carbonization and oxidation transformed ZIF-8@GO into metallic-Zn-doped carbon on graphene (ZDC@G). Finally, a polymer was grafted onto the sp^2 carbon skeletons via FRP as photothermally-responsive polymer brushes (TRB) to yield TRB-ZnO@G. Under NIR irradiation, the adequately water-dispersed 1-μm-sized hydrophilic TRB-ZnO@G (25 °C) was transformed into 10-μm-sized hydrophobic aggregates for generating hyperthermia (56 °C) (**Figure 11b**). The phase-to-size-transformation phenomenon was further explored for eradicating multiple bacteria (*E. coli* and *S. aureus*). A bactericidal efficacy of 100% was achieved at a low dose (50 μg mL^{-1}), which was caused by wrapping the surrounding local bacteria into the micrometer-sized aggregates for 5 min of NIR-light-enabled hyperthermia, physical cutting, and enhanced Zn^{2+}-ion penetration. Moreover, the modified carbon nanosheets exhibited rapid and safe skin-wound-disinfection capabilities.

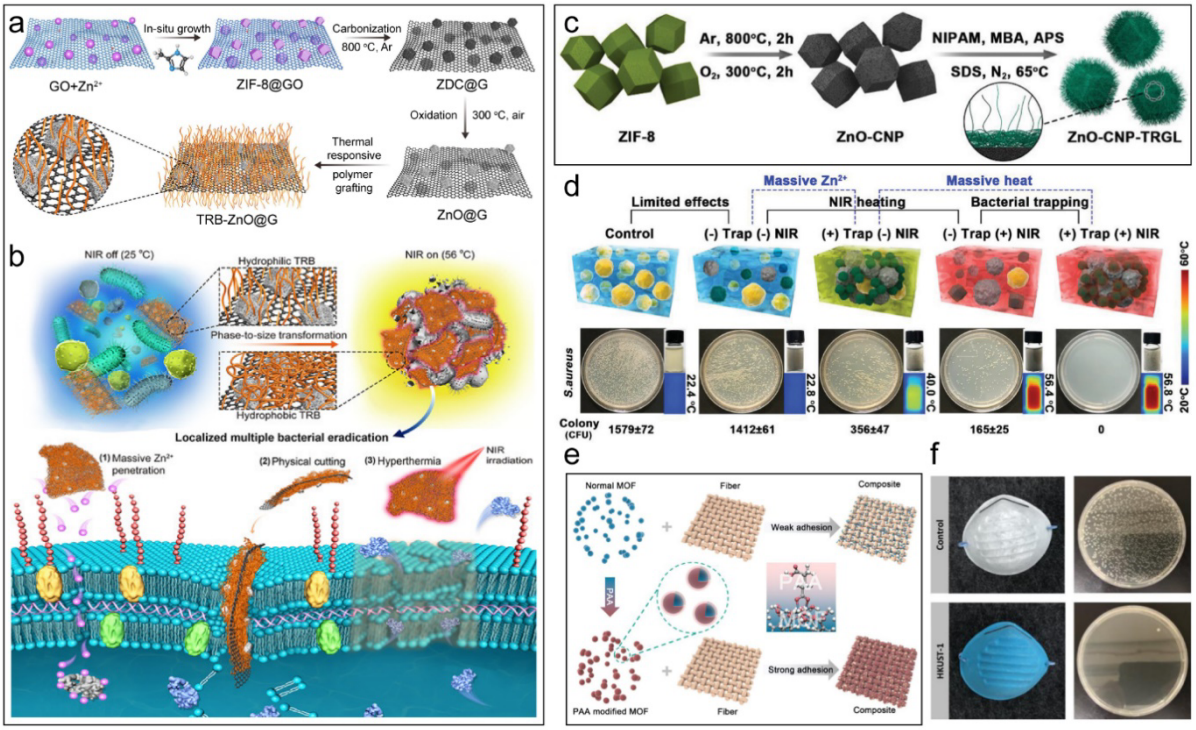

Figure 11. Development and operation of TRB-ZnO@G, ZnO-CNP-TRGL, and HKUST/cotton composites for inducing antibacterial effects. (a) Construction of MOF-derived carbon nanosheets modified with a thermally responsive polymer brush layer (TRB-ZnO@G) for bacterial eradication. (b) Illustration depicting the aggregation mediated by phase-to-size transformation and the triple-modal-activated antibacterial activity. Reproduced with permission.[141] Copyright 2019, American Chemical Society. (c) Synthesis of ZnO-CNP-TRGL with in situ polymerized PNIPAM for synergistic chemo-photothermal bacterial disinfection. (d) Five experimental groups with *S. aureus* bacterial agar plates, and photothermal images acquired under laser irradiation (808 nm; 2 W cm^{-2}). Reproduced with permission.[142] Copyright 2019, Wiley-VCH. (e) Schematic of MOF–fiber composites. (f) Comparison of bacterial amounts before and after treatment with the HKUST/cotton-40 composite. Reproduced with permission.[137] Copyright 2021, Wiley-VCH.

In another study conducted by the same research group, NIR-responsive size-transformable on–off switching was engineered to prepare smart MOF-nanocarbons for chemo-photothermal bacterial disinfection.[142] ZnO-doped carbon nanoparticles (CNPs) were prepared by carbonization using ZIF-8 as the precursor (**Figure 11c**). Thereafter, a PNIPAM-based thermoresponsive gel layer (TRGL) was coated onto the surface via in situ polymerization to form nanocarbon–bacteria aggregates. ZnO-CNP-TRGLs with different sizes (25, 50, 100, and 1000 nm) were prepared, and their photo-to-thermal conversion

abilities and Zn^{2+}-release-associated chemotherapeutic activities were evaluated. The low-dosage ZnO-CNP-TRGLs mediated the bacterial ablation with 100% efficiency under NIR irradiation, highlighting the robustness and localization of this antibacterial approach (**Figure 11d**).

As discussed earlier, prolonged bacterial infections arising from antibiotic-resistant bacteria are a significant public health hazard. With a focus on developing a water-stable material that could repel harmful pathogens, Neufeld et al. prepared a Cu-BTTri ($(H_3[(Cu_4Cl)_3\text{-}(BTTri)_8]$ (H_3BTTri: 1,3,5-tris(1H-1,2,3-triazole-5-yl)benzene)) chitosan matrix (chitosan/Cu-BTTri).[143] *P. aeruginosa* was selected for bacterial attachment owing to its prevalence in biofilms and high antibiotic resistance.[144] After bacterial exposure for 6 h, the chitosan/Cu-BTTri films exhibited a 81%–87% reduction in the attachment of live bacteria, which was maintained even after 24 h of exposure, suggesting their reusability. The control chitosan films, which also exhibited antibacterial properties, reduced the attachment by 55%–65%, which further decreased to below 34% after 24 h.

Studies have been conducted to couple MOFs with polymer fibers and textiles to expand the scope of polymers. MOFs can be incorporated into clothing to endure harmful real-world conditions such as toxic chemicals, infectious agents, and fire. Three archetypal MOFs—HKUST-1, UiO-66-NH_2, and ZIF-8—have been extensively used in conjugation with polymers such as polyacrylonitrile, polypropylene, nylon, PS, PVDF, and PVA to generate MOF–fabric systems.[145] These systems can also be used in healthcare-related protective wearables, such as clothing and masks. We recently prepared MOF–fiber composites of HKUST-1 with a variety of fabric materials using a drip-casting approach for antibacterial applications (**Figure 11e,f**).[146] Coordinative interactions between PAA and the MOF substrates were crucial in holding the composites together, as indicated by DFT calculations.

4.5. Anti-Oxidation and Anti-Inflammation Behavior. In addition to their roles in ablating bacteria, tumor cells, and tissues, SAEs—which are a subclass of MOFs—could be utilized for antioxidative therapy to protect normal cells by scavenging overexpressed ROS.[147] Inspired by the operation of natural enzymes, Ma et al. prepared N-doped porous carbon anchored with Fe single-atoms (Fe-SAs/NC) through pyrolysis of Fe-phthalocyanine-encapsulated ZIF-8 to scavenge ROS.[148] As a catalase-mimicking enzyme, the single-atom Fe-SAs/NC decomposed H_2O_2 into H_2O and O_2, as evidenced by CV and O_2-generation assays. Thereafter, the superoxide dismutase activity was verified by the inhibition of formazan dye upon reacting with $O_2^{\bullet-}$. For intracellular ROS scavenging in

HeLa cells, Fe-SAs/NC was encapsulated with DSPE-PEG (1,2-distearoyl-*sn*-glycero-3-phosphoethanolamine-N-(methoxy(polyethyleneglycol)), Mw 2000). To monitor the changes in ROS in the HeLa cells, pre-incubation with β-lapachone (6 h before analysis) was performed for the control case and pre-treatment with Fe-SAs/NC. Interestingly, a significant 6.8-fold reduction in oxidative stress was observed for the cells pre-treated with 30 μg mL^{-1} SAEs. Moreover, the SAEs showed 85% HeLa cell survival compared to that of the control (N-doped carbon; NC).

In another study, Li et al. used F127 and $PEO_{106}PPO_{70}PEO_{106}$ as templating agents to prepare hierarchical microporous Zr-based UiO-66-NH_2 for developing a biomimetic antioxidant defense system (**Figure 12a**).[149] Natural SOD was loaded into the 7-nm-sized micropores generated by the Hofmeister ClO_4^--mediated F127-templated HMUiO-66-NH_2, with a CAT-mimicking Mn/porphyrin-doped framework. Cell viability was determined after overexpressing oxidative stress using paraquat. Surprisingly, the SOD@HMUiO-MnTCPP composite provided optimal protection to the HeLa cells from ROS. Other treatment groups such as only HMUiO-66-NH_2, HMUiO-MNTCPP, and unattached SOD showed minor changes in protection, suggesting the importance of the co-loaded natural SOD and CAT enzymes. Moreover, SOD@HMUiO-MnTCPP showed weakened green fluorescence (**Figure 12b**). Furthermore, the expression levels of p-p38 mitogen-activated protein kinase (MAPK) and cyclooxygenase-2 (COX-2) in physiological cell damage were monitored using western blotting (**Figure 12c**). Dramatically reduced expression levels were observed for the prepared nanosystem. The introduction of biomaterials clearly elicited physiological inflammatory responses accompanied by pro-inflammatory cytokine release, resulting in osseointegration failure. Therefore, locally acting anti-inflammatory agents must be developed in this regard.

Kang et al. fabricated exosome-functionalized PLGA/Mg-GA-MOF-based nanofibrous scaffolds for anti-inflammatory and related applications (**Figure 12d**).[150] Initially, a blend of poly(lactic-co-glycolic acid) (PLGA) and the Mg-gallic acid (GA) MOF was electrospun to form a positively charged PLGA/Mg-GA-MOF scaffold. Thereafter, negatively charged exosomes extracted from human adipose-derived stem cells were deposited. Electrospun PLGA is a popular choice for implantable devices owing to its biocompatibility, tunable mechanical properties, and ability to stimulate cell–matrix interactions, thereby creating cell niches. Anti-inflammatory activity was evaluated using RAW264.7 cells by assessing the expression of COX-2 and inducible nitric oxide synthase (iNOS) upon release of Mg^{2+}, GA, and exosomes. PLGA/Mg-GA exhibited the lowest expression of both iNOS and COX-2 among the investigated groups owing to the release of bioactive molecules to modulate

immune responses (**Figure 12e**).

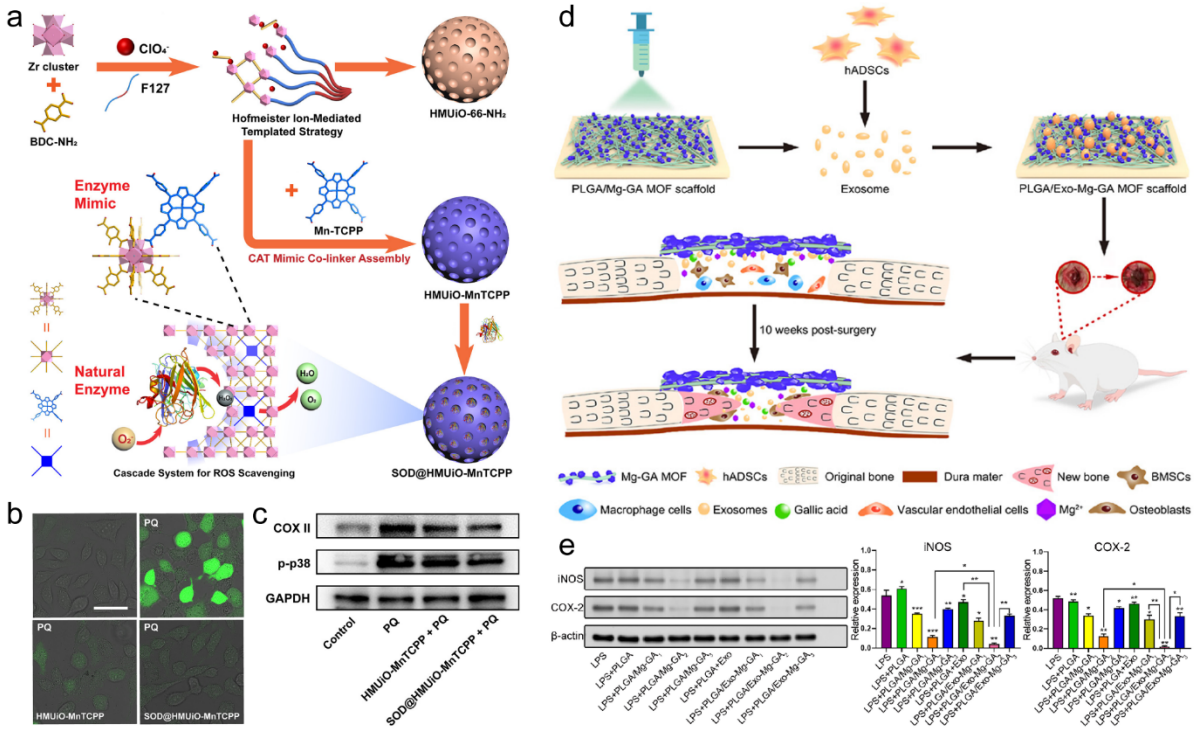

Figure 12. Design and operation of SOD@HMUiO-MnTCPP and PLGA/Exo-Mg-GA exhibiting anti-oxidative and anti-inflammatory effects. (a) Schematic illustrating the synthesis of an SOD@HMUiO-MnTCPP mesoMOF via the F127-polymer-mediated Hofmeister-ion-template strategy for devising a cascade ROS-scavenging system. (b) HeLa cells with an ROS fluorescent probe subjected to different treatments (scale bar: 50 μm). (c) Western blot expression levels of COX-II and p-p38. Reproduced with permission.[149] Copyright 2021, American Chemical Society. (d) Schematic of the PLGA/Exo-Mg-GA MOF scaffold. (e) Expression levels of iNOS and COX-II using western blot analysis. (*p<0.05; **p<0.01; ***p<0.001). Reproduced with permission.[150] Copyright 2022, Elsevier.

4.6. Environmental Protection. The global climate has vastly deteriorated since the industrial revolution and globalization. Humans and other species face many issues arising from air and water pollution. Particulate matter (PM) with aerodynamic diameters of less than 2.5 μm ($PM_{2.5}$) and 10 μm (PM_{10}) poses serious health risks as it can enter the respiratory tract via air passages. Several outdoor gaseous pollutants, such as sulfur dioxides, nitrogen oxides, carbon monoxide, and chlorofluorocarbons, have also been responsible for disrupting the forest ecosystem and impacting human health. Wang et al. developed a series of MOF filters based on ZIF-8, UiO-66-NH_2, MOF-199, and Mg-MOF-74 along with polymers such as polyacrylonitrile (PAN), PS, and PVP (**Figure 13a**).[151] Using the electrospinning technique

with tunable parameters such as the electric voltage and solution flow rate, MOFs were spun into fiber mats with the polymers. ZIF-8/PAN and UiO-66-NH_2/PAN were highly effective against the air pollutants PM and SO_2, respectively. The ZIF-8/PAN filter remarkably achieved 88.33% ± 1.52% $PM_{2.5}$ removal and 89.67 ± 1.33% PM_{10} removal (**Figure 13b**). The highly positive zeta potential (47.5) that was due to unbalanced metal ions and surface defects on ZIF-8 polarized the PM, thereby enhancing its attachment onto the MOF filters (**Figure 13c**). ZIF-8/PAN maintained decent performance upon prolonged exposure (48 h) to the pollutants. However, UiO-66-NH_2/PAN with 60% MOF loading adsorbed SO_2 at a capacity of 0.019 g with a low-pressure drop of 20 Pa (**Figure 13d**). Given the acidic and polar nature of SO_2, the UiO-66-NH_2 MOF with its inherent polar, basic functional groups also operated effectively under highly humid conditions. This study revealed the importance of incorporating MOFs into polymeric materials for efficient pollutant and gas capture. Apart from air-pollutant-filtering systems, nerve agents have been successfully treated using MOF hybrids. Focusing on the remarkable effectiveness of immobilized enzymes, Farha et al. used a water-stable MOF PCN-128y to load organophosphorus acid anhydrolase (OPAA), yielding OPAA@PCN-128y.[152] OPAA, a catalyzing enzyme for bonds such as P–F, P–O, P–CN, was encapsulated into the mesopores of PCN-128y (12 wt%). Then, O-pinacolyl methyl fluorophosponate (Soman), a deadly G-type nerve agent (3 mM), was hydrolyzed by 90% in an hour using 3.75 μg of OPAA@PCN-128y, leading to its deactivation (defluorination). These inspiring results indicate the feasibility of using enzyme-immobilized MOFs for decontamination.

MOFs or polymers have been used to tackle water pollution through approaches including wastewater treatment based on removing organic contaminants and recovering commodities. Owing to their porous nature, large surface area, and flexibility, MOFs have been utilized for recycling and recovering precious metals, as well as sequestering heavy metal ions. However, in reality, the issues of long-term stability of MOFs and the insubstantial rigidity and regularity of the polymers prevent their implementation in industrial settings. MOF–polymer blends have been explored as promising systems to remove contaminants such as methylchlorophenoxypropionic acid, methylene blue, rhodamine, tetracycline, and bacterial inactivation.[153–157] Recent reports from Queen et al. highlight the benefits of using MOF–polymer hybrids. A redox-active MOF–polymer composite combining MIL-100(Fe) [Fe-BTC; BTC = 1,3,5-benzenetricarboxylate] and PDA was prepared to extract Pb^{2+}, Pd^{2+}, and Hg^{2+} from freshwater reservoirs.[158,159] The same porous MOF (Fe-BTC) was subsequently combined with a series of polymer building blocks such as polyhydroquinone

(PHQ), poly(para-phenylenediamine) (PpPDA), polytyramine (PTA), and poly(meta-aminophenol) (PmAP) to extract gold.[160] Record Au^{3+} extraction (23.9 K) and removal capacity (934 mg gold g^{-1}) were achieved within 2 min of equilibration. The exceptional sequestration rates were ascribed to the introduction of additional open-metal-site porosity into the redox-active polymers.

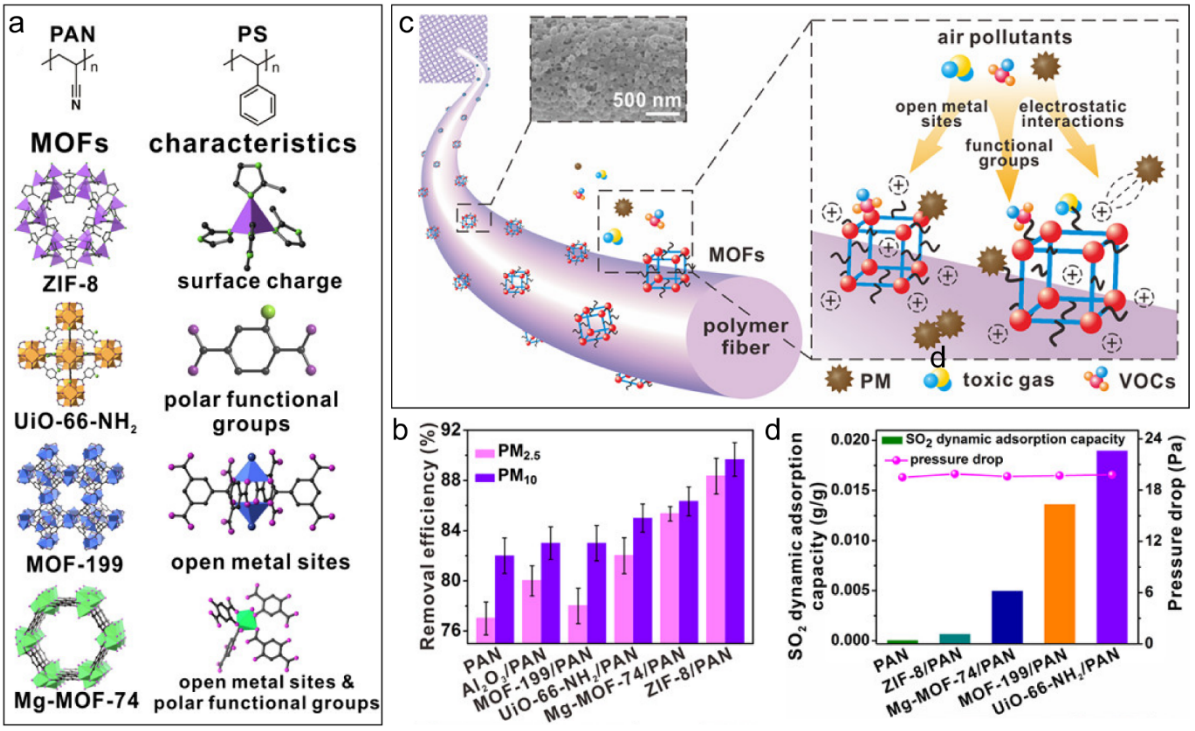

Figure 13. PAN–MOF filters used for pollutant removal. (a) Chemical and crystalline structures of the polymers and MOFs. (b) Study of PAN–MOF filter composites and other controls for PM removal. (c) Proposed mechanism of MOF filters used for environmental pollution control. (d) SO_2 adsorption from a SO_2/NO_2 mixture with a flow rate of 50 mL min^{-1}. Reproduced with permission.[151] Copyright 2016, American Chemical Society

5. Conclusion and Outlook

This review comprehensively summarizes recent advances in the preparation and applications of MOF–polymer hybrids. The increasing body of literature on MOF–polymer hybridization suggests its popularity as a research front. Depending on the stage of MOF preparation, polymers can be incorporated to alter the overall properties. Polymerization within nanochannels is an in situ preparation method that involves introducing guest monomers into the MOF pores, yielding porous materials. However, the challenges involved in controlling the polymer weight and loading amounts have directed researchers toward post-translating MOFs with preformed polymers. Polymer shells can be constructed around MOFs using

covalent grafting techniques, which have their own advantages and limitations. PolyMOFs—a separate class of MOFs produced using bottom-up hybridization techniques—remain in their infancy, and the architectural interplay between their components has not been clarified. Nevertheless, considerable efforts have been made toward understanding the interactions between the hard (MOF) and soft (polymer) materials to prepare unique systems capable of solving various global problems, such as multimodal anticancer theranostics; biomedical imaging and sensing; air and water pollution remediation; catalysis; and gas separation.

Despite the plethora of advantages offered by the amalgamation of MOFs and polymers, certain critical issues impede the development of MOF–polymer hybrids suitable for practical applications.

1. Numerous studies have revealed the close relationship between structure and performance. Research pertaining to features such as MOF crystal size and pore size, degree of polymerization, and interactions between MOFs and polymers can help elucidate mass transport and diffusion. To further clarify the structure–activity relationships for both MOFs and polymers, advanced characterization tools must be supported with simulations and mathematical-modeling approaches.
2. Although the introduction of polymers enhances the functionality and versatility of MOF templates, issues concerning polymer loading and maintaining homogeneity warrant further research. Polymer loading levels could impact the bilateral flow of targeted guest molecules, which can reduce the porosity and accessibility to active sites within the MOF architecture. Thus, new strategies should be devised to enhance the spatial distribution and interfacial interactions.
3. In polymer self-assembly, the polymer is assumed to be a simple chain-shaped molecule with averaged-out features for convenience, as it is difficult to precisely determine the atomic-level polymer structure. However, in reality, elongated polymer chains are isolated and immobilized.
4. The molecular sieving feature of MOFs enables them to act as gas separators. Consequently, a clear understanding of their structure and performance is crucial. Reliable methods such as focused-ion-beam/SEM tomography could provide insight into the filler distribution and interfacial contact.
5. Considering the individual applications of MOFs or polymers in developing photoenergy conversion devices, the photoelectric synergy of MOF–polymer hybrids could produce optimized nanosystems. Spatial control over donor–acceptor interfaces could result in well-defined photoinduced charge and energy transfer.

6. Ample research has been conducted on proof-of-concepts for applications such as gas separation and the capture and degradation of chemical warfare agents. Although these studies are a critical steppingstone, they should be aimed at mimicking actual field conditions. Testing the prepared materials in accurate replicas of the investigated systems is paramount to validating their utility.

7. Although certain hybrid systems have been used in public-health-related areas, research in this regard falls remarkably short of being applicable to the actual clinical translation stage, mostly owing to concerns over biocompatibility. More long-term in-depth studies must be conducted to assess adsorption–distribution–metabolism–excretion processes. To mitigate concerns related directly to MOF use, endogenous metal centers should be employed. Finally, the difficulty in achieving rapid, robust, and reproducible large-scale production should be overcome to facilitate clinical applications.

Although this developing field has several challenges, its potential is highlighted by the numerous efforts devoted to the rational design and integration of MOFs and polymers. With a better understanding of MOF–polymer interfaces, regulated polymer addition, and improved chemical and mechanical stability, next-generation biosafe MOF–polymer hybrids can be constructed. Persistent efforts, innovative strategies, and cutting-edge technologies in the coming years are anticipated to propel the exciting frontier of MOF–polymer hybrid chemistry.

Acknowledgements

This research work was supported by the Singapore Agency for Science, Technology and Research (A*STAR) AME IRG grant (A20E5c0081) and the Singapore National Research Foundation Investigatorship (NRF-NRFI2018-03).

References

[1] M. X. Wu, Y. W. Yang, *Adv. Mater.* **2017**, *29*, 1606134.

[2] X. Wang, J. Zhou, H. Fu, W. Li, X. Fan, G. Xin, J. Zheng, X. Li, *J. Mater. Chem. A* **2014**, *2*, 14064.

[3] J. Yang, F. Zhang, H. Lu, X. Hong, H. Jiang, Y. Wu, Y. Li, *Angew. Chem. Int. Ed.* **2015**, *54*, 10889.

[4] W. W. Zhan, Q. Kuang, J. Z. Zhou, X. J. Kong, Z. X. Xie, L. S. Zheng, *J. Am. Chem. Soc.* **2013**, *135*, 1926.

[5] G. Li, H. Kobayashi, J. M. Taylor, R. Ikeda, Y. Kubota, K. Kato, M. Takata, T.

Yamamoto, S. Toh, S. Matsumura, H. Kitagawa, *Nat. Mater.* **2014**, *13*, 802.

[6] J. S. Qin, D. Y. Du, W. Guan, X. J. Bo, Y. F. Li, L. P. Guo, Z. M. Su, Y. Y. Wang, Y. Q. Lan, H. C. Zhou, *J. Am. Chem. Soc.* **2015**, *137*, 7169.

[7] A. A. Talin, A. Centrone, A. C. Ford, M. E. Foster, V. Stavila, P. Haney, R. A. Kinney, V. Szalai, F. El Gabaly, H. P. Yoon, F. Léonard, M. D. Allendorf, *Science* **2014**, *343*, 66.

[8] M. Kim, J. F. Cahill, H. Fei, K. A. Prather, S. M. Cohen, *J. Am. Chem. Soc.* **2012**, *134*, 18082.

[9] H. Furukawa, F. Gándara, Y. B. Zhang, J. Jiang, W. L. Queen, M. R. Hudson, O. M. Yaghi, *J. Am. Chem. Soc.* **2014**, *136*, 4369.

[10] P. Horcajada, T. Chalati, C. Serre, B. Gillet, C. Sebrie, T. Baati, J. F. Eubank, D. Heurtaux, P. Clayette, C. Kreuz, J. S. Chang, Y. K. Hwang, V. Marsaud, P. N. Bories, L. Cynober, S. Gil, G. Ferey, P. Couvreur, R. Gref, *Nat. Mater.* **2010**, *9*, 172.

[11] Z. Jiang, X. Xu, Y. Ma, H. S. Cho, D. Ding, C. Wang, J. Wu, P. Oleynikov, M. Jia, J. Cheng, Y. Zhou, O. Terasaki, T. Peng, L. Zan, H. Deng, *Nature* **2020**, *586*, 549.

[12] A. Aijaz, A. Karkamkar, Y. J. Choi, N. Tsumori, E. Rönnebro, T. Autrey, H. Shioyama, Q. Xu, *J. Am. Chem. Soc.* **2012**, *134*, 13926.

[13] X. Wang, L. Yu, B. Y. Guan, S. Song, X. W. Lou, *Adv. Mater.* **2018**, *30*, 1801211.

[14] W. Ahn, M. G. Park, D. U. Lee, M. H. Seo, G. Jiang, Z. P. Cano, F. M. Hassan, Z. Chen, *Adv. Funct. Mater.* **2018**, *28*, 1802129.

[15] N. Stock, S. Biswas, *Chem. Rev.* **2012**, *112*, 933.

[16] H. B. Tanh Jeazet, C. Staudt, C. Janiak, *Dalton Trans.* **2012**, *41*, 14003.

[17] Y. Z. Chen, Y. X. Zhou, H. Wang, J. Lu, T. Uchida, Q. Xu, S. H. Yu, H. L. Jiang, *ACS Catal.* **2015**, *5*, 2062.

[18] J. Chang, X. Wang, J. Wang, H. Li, F. Li, *Anal. Chem.* **2019**, *91*, 3604.

[19] G. Chen, S. Huang, X. Kou, S. Wei, S. Huang, S. Jiang, J. Shen, F. Zhu, G. Ouyang, *Angew. Chem. Int. Ed.* **2019**, *58*, 1463.

[20] B. Wang, X. L. Lv, D. Feng, L. H. Xie, J. Zhang, M. Li, Y. Xie, J. R. Li, H. C. Zhou, *J. Am. Chem. Soc.* **2016**, *138*, 6204.

[21] K. Wang, S. Wang, J. Liu, Y. Guo, F. Mao, H. Wu, Q. Zhang, *ACS Appl. Mater. Interfaces* **2021**, *13*, 15315.

[22] C. Li, K. Wang, J. Li, Q. Zhang, *Nanoscale* **2020**, *12*, 7870.

[23] K. Wang, Y. Guo, Q. Zhang, *Small Struct.* **2022**, *3*, 2100115.

[24] Z. Y. Gu, C. X. Yang, N. Chang, X. P. Yan, *Acc. Chem. Res.* **2012**, *45*, 734.

[25] L. Shang, H. Yu, X. Huang, T. Bian, R. Shi, Y. Zhao, G. I. N. Waterhouse, L. Z. Wu, C.

H. Tung, T. Zhang, *Adv. Mater.* **2016**, *28*, 1668.

[26] Z. Chen, R. Wu, Y. Liu, Y. Ha, Y. Guo, D. Sun, M. Liu, F. Fang, *Adv. Mater.* **2018**, *30*, 1802011.

[27] X. Lian, Y. Fang, E. Joseph, Q. Wang, J. Li, S. Banerjee, C. Lollar, X. Wang, H. C. Zhou, *Chem. Soc. Rev.* **2017**, *46*, 3386.

[28] L. B. Vilhelmsen, K. S. Walton, D. S. Sholl, *J. Am. Chem. Soc.* **2012**, *134*, 12807.

[29] N. Nurxat, B. Hanying, S. Kai, *Prog. Polym. Sci.* **2013**, *38*, 302.

[30] M. Kalaj, K. C. Bentz, S. Ayala, J. M. Palomba, K. S. Barcus, Y. Katayama, S. M. Cohen, *Chem. Rev.* **2020**, *120*, 8267.

[31] Y. Jing, Y. Yoshida, P. Huang, H. Kitagawa, *Angew. Chem. Int. Ed.* **2022**, *61*, e202117417.

[32] J. Jiang, Y. Zhao, O. M. Yaghi, *J. Am. Chem. Soc.* **2016**, *138*, 3255.

[33] A. Carné-Sánchez, K. C. Stylianou, C. Carbonell, M. Naderi, I. Imaz, D. Maspoch, *Adv. Mater.* **2015**, *27*, 869.

[34] W. Zhang, Y. Hu, J. Ge, H. L. Jiang, S. H. Yu, *J. Am. Chem. Soc.* **2014**, *136*, 16978.

[35] B. Le Ouay, S. Kitagawa, T. Uemura, *J. Am. Chem. Soc.* **2017**, *139*, 7886.

[36] Y. Yang, J. Liu, C. Liang, L. Feng, T. Fu, Z. Dong, Y. Chao, Y. Li, G. Lu, M. Chen, Z. Liu, *ACS Nano* **2016**, *10*, 2774.

[37] S. K. Bhardwaj, N. Bhardwaj, G. C. Mohanta, P. Kumar, A. L. Sharma, K. H. Kim, A. Deep, *ACS Appl. Mater. Interfaces* **2015**, *7*, 26124.

[38] E. Barea, C. Montoro, J. A. R. Navarro, *Chem. Soc. Rev.* **2014**, *43*, 5419.

[39] K. Shen, X. Chen, J. Chen, Y. Li, *ACS Catal.* **2016**, *6*, 5887.

[40] M. Zhao, K. Yuan, Y. Wang, G. Li, J. Guo, L. Gu, W. Hu, H. Zhao, Z. Tang, *Nature* **2016**, *539*, 76.

[41] L. Wang, Y. Han, X. Feng, J. Zhou, P. Qi, B. Wang, *Coord. Chem. Rev.* **2016**, *307*, 361.

[42] J. Chen, F. Xue, W. Du, H. Yu, Z. Yang, Q. Du, H. Chen, *Nano Lett.* **2022**, *22*, 6156.

[43] J. Shen, H. Yu, Y. Shu, M. Ma, H. Chen, *Adv. Funct. Mater.* **2021**, *31*, 2106106.

[44] L. M. Robeson, Q. Liu, B. D. Freeman, D. R. Paul, *J. Memb. Sci.* **2015**, *476*, 421.

[45] L. Cao, K. Tao, A. Huang, C. Kong, L. Chen, *Chem. Commun.* **2013**, *49*, 8513.

[46] N. C. Su, D. T. Sun, C. M. Beavers, D. K. Britt, W. L. Queen, J. J. Urban, *Energy Environ. Sci.* **2016**, *9*, 922.

[47] M. S. Denny, S. M. Cohen, *Angew. Chem. Int. Ed.* **2015**, *54*, 9029.

[48] H. Wang, S. He, X. Qin, C. Li, T. Li, *J. Am. Chem. Soc.* **2018**, *140*, 17203.

[49] M. D. Rowe, C. C. Chang, D. H. Thamm, S. L. Kraft, J. F. Harmon, A. P. Vogt, B. S.

Sumerlin, S. G. Boyes, *Langmuir* **2009**, *25*, 9487.

[50] M. D. Rowe, D. H. Tham, S. L. Kraft, S. G. Boyes, *Biomacromolecules* **2009**, *10*, 983.

[51] A. Zimpel, T. Preiß, R. Röder, H. Engelke, M. Ingrisch, M. Peller, J. O. Rädler, E. Wagner, T. Bein, U. Lächelt, S. Wuttke, *Chem. Mater.* **2016**, *28*, 3318.

[52] K. Xie, Q. Fu, Y. He, J. Kim, S. J. Goh, E. Nam, G. G. Qiao, P. A. Webley, *Chem. Commun.* **2015**, *51*, 15566.

[53] K. A. McDonald, J. I. Feldblyum, K. Koh, A. G. Wong-Foy, A. J. Matzger, *Chem. Commun.* **2015**, *51*, 11994.

[54] N. Abdelmageed, W. A. El-Said, A. A. Younes, M. S. Atrees, A. B. Farag, E. A. Elshehy, A. M. Abdelkader, *J. Appl. Polym. Sci.* **2021**, *138*, e51263.

[55] D. Zhao, Q. Huo, J. Feng, B. F. Chmelka, G. D. Stucky, *J. Am. Chem. Soc.* **1998**, *120*, 6024.

[56] J. Yao, M. He, K. Wang, R. Chen, Z. Zhong, H. Wang, *CrystEngComm* **2013**, *15*, 3601.

[57] D. Wang, H. Wu, S. Z. F. Phua, G. Yang, W. Qi Lim, L. Gu, C. Qian, H. Wang, Z. Guo, H. Chen, Y. Zhao, *Nat. Commun.* **2020**, *11*, 357.

[58] J. Hwang, T. Heil, M. Antonietti, B. V. K. J. Schmidt, *J. Am. Chem. Soc.* **2018**, *140*, 2947.

[59] N. Yanai, T. Uemura, S. Kitagawa, *Chem. Mater.* **2012**, *24*, 4744.

[60] T. Uemura, N. Yanai, S. Watanabe, H. Tanaka, R. Numaguchi, M. T. Miyahara, Y. Ohta, M. Nagaoka, S. Kitagawa, *Nat. Commun.* **2010**, *1*, 83.

[61] T. Kitao, S. Bracco, A. Comotti, P. Sozzani, M. Naito, S. Seki, T. Uemura, S. Kitagawa, *J. Am. Chem. Soc.* **2015**, *137*, 5231.

[62] Y. Chen, V. Lykourinou, C. Vetromile, T. Hoang, L. J. Ming, R. W. Larsen, S. Ma, *J. Am. Chem. Soc.* **2012**, *134*, 13188.

[63] P. Li, J. A. Modica, A. J. Howarth, E. Vargas L., P. Z. Moghadam, R. Q. Snurr, M. Mrksich, J. T. Hupp, O. K. Farha, *Chem* **2016**, *1*, 154.

[64] K. Liang, R. Ricco, C. M. Doherty, M. J. Styles, S. Bell, N. Kirby, S. Mudie, D. Haylock, A. J. Hill, C. J. Doonan, P. Falcaro, *Nat. Commun.* **2015**, *6*, 7240.

[65] T. T. Chen, J. T. Yi, Y. Y. Zhao, X. Chu, *J. Am. Chem. Soc.* **2018**, *140*, 9912.

[66] X. Yang, Q. Tang, Y. Jiang, M. Zhang, M. Wang, L. Mao, *J. Am. Chem. Soc.* **2019**, *141*, 3782.

[67] C. A. Allen, J. A. Boissonnault, J. Cirera, R. Gulland, F. Paesani, S. M. Cohen, *Chem. Commun.* **2013**, *49*, 3200.

[68] Z. Zhang, H. T. H. Nguyen, S. A. Miller, S. M. Cohen, *Angew. Chem. Int. Ed.* **2015**, *54*,

6152.

[69] S. Ayala, Z. Zhang, S. M. Cohen, *Chem. Commun.* **2017**, *53*, 3058.

[70] Z. Zhang, H. T. H. Nguyen, S. A. Miller, A. M. Ploskonka, J. B. Decoste, S. M. Cohen, *J. Am. Chem. Soc.* **2016**, *138*, 920.

[71] P. G. M. Mileo, S. Yuan, S. Ayala, P. Duan, R. Semino, S. M. Cohen, K. Schmidt-Rohr, G. Maurin, *J. Am. Chem. Soc.* **2020**, *142*, 10863.

[72] M. A. Pearson, M. Dincă, J. A. Johnson, *Chem. Mater.* **2021**, *33*, 9508.

[73] A. Zimpel, N. Al Danaf, B. Steinborn, J. Kuhn, M. Höhn, T. Bauer, P. Hirschle, W. Schrimpf, H. Engelke, E. Wagner, M. Barz, D. C. Lamb, U. Lächelt, S. Wuttke, *ACS Nano* **2019**, *13*, 3884.

[74] L. Hu, C. Xiong, G. Wei, Y. Yu, S. Li, X. Xiong, J. J. Zou, J. Tian, *J. Colloid Interface Sci.* **2022**, *608*, 1882.

[75] Y. Yang, L. Xu, W. Zhu, L. Feng, J. Liu, Q. Chen, Z. Dong, J. Zhao, Z. Liu, M. Chen, *Biomaterials* **2018**, *156*, 121.

[76] Y. Liu, C. S. Gong, Y. Dai, Z. Yang, G. Yu, Y. Liu, M. Zhang, L. Lin, W. Tang, Z. Zhou, G. Zhu, J. Chen, O. Jacobson, D. O. Kiesewetter, Z. Wang, X. Chen, *Biomaterials* **2019**, *218*, 119365.

[77] J. Gandara-Loe, B. E. Souza, A. Missyul, G. Giraldo, J. C. Tan, J. Silvestre-Albero, *ACS Appl. Mater. Interfaces* **2020**, *12*, 30189.

[78] M. Giménez-marqués, E. Bellido, T. Berthelot, T. Simón-yarza, T. Hidalgo, R. Simón-vázquez, Á. González-fernández, J. Avila, M. C. Asensio, R. Gref, P. Couvreur, C. Serre, P. Horcajada, *Small* **2018**, *14*, 1801900.

[79] Y. Ding, H. Xu, C. Xu, Z. Tong, S. Zhang, Y. Bai, Y. Chen, Q. Xu, L. Zhou, H. Ding, Z. Sun, S. Yan, Z. Mao, W. Wang, *Adv. Sci.* **2020**, *7*, 2001060.

[80] Z. He, X. Huang, C. Wang, X. Li, Y. Liu, Z. Zhou, S. Wang, F. Zhang, Z. Wang, O. Jacobson, J. J. Zhu, G. Yu, Y. Dai, X. Chen, *Angew. Chem. Int. Ed.* **2019**, *58*, 8752.

[81] D. Duan, H. Liu, M. Xu, M. Chen, Y. Han, Y. Shi, Z. Liu, *ACS Appl. Mater. Interfaces* **2018**, *10*, 42165.

[82] K. Kim, S. Lee, E. Jin, L. Palanikumar, J. H. Lee, J. C. Kim, J. S. Nam, B. Jana, T. H. Kwon, S. K. Kwak, W. Choe, J. H. Ryu, *ACS Appl. Mater. Interfaces* **2019**, *11*, 27512.

[83] W. Ni, J. Wu, H. Fang, Y. Feng, Y. Hu, L. Lin, J. Chen, F. Chen, H. Tian, *Nano Lett.* **2021**, *21*, 7796.

[84] J. Shen, M. Ma, M. Shafiq, H. Yu, Z. Lan, H. Chen, *Angew. Chem. Int. Ed.* **2022**, *61*, e202113703.

[85] L. Zhao, Y. Liu, R. Chang, R. Xing, X. Yan, *Adv. Funct. Mater.* **2019**, *29*, 1806877.

[86] E. B. Dickerson, E. C. Dreaden, X. Huang, I. H. El-Sayed, H. Chu, S. Pushpanketh, J. F. McDonald, M. A. El-Sayed, *Cancer Lett.* **2008**, *269*, 57.

[87] K. Novak, *Nat. Rev. Cancer* **2003**, *3*, 887.

[88] G. Fu, W. Liu, S. Feng, X. Yue, *Chem. Commun.* **2012**, *48*, 11567.

[89] W. Zhu, K. Liu, X. Sun, X. Wang, Y. Li, L. Cheng, Z. Liu, *ACS Appl. Mater. Interfaces* **2015**, *7*, 11575.

[90] Y. Liu, G. Shu, X. Li, H. Chen, B. Zhang, H. Pan, T. Li, X. Gong, H. Wang, X. Wu, Y. Dou, J. Chang, *Adv. Funct. Mater.* **2018**, *28*, 1802026.

[91] J. Wang, F. Guo, M. Yu, L. Liu, F. Tan, R. Yan, N. Li, *J. Controlled Release* **2016**, *237*, 23.

[92] K. Yang, H. Xu, L. Cheng, C. Sun, J. Wang, Z. Liu, *Adv. Mater.* **2012**, *24*, 5586.

[93] S. Li, L. Zhang, X. Liang, T. Wang, X. Chen, C. Liu, L. Li, C. Wang, *Chem. Eng. J.* **2019**, *378*, 122175.

[94] D. Wang, H. Wu, J. Zhou, P. Xu, C. Wang, R. Shi, H. Wang, H. Wang, Z. Guo, Q. Chen, *Adv. Sci.* **2018**, *5*, 1800287.

[95] A. K. Bindra, D. Wang, Z. Zheng, D. Jana, W. Zhou, S. Yan, H. Wu, Y. Zheng, Y. Zhao, *Biomaterials* **2021**, *279*, 121188.

[96] W. Wang, L. Wang, Y. Li, S. Liu, Z. Xie, X. Jing, *Adv. Mater.* **2016**, *28*, 9320.

[97] X. Cai, X. Deng, Z. Xie, Y. Shi, M. Pang, J. Lin, *Chem. Eng. J.* **2019**, *358*, 369.

[98] J. Huang, N. Li, C. Zhang, Z. Meng, *ACS Appl. Mater. Interfaces* **2018**, *10*, 38729.

[99] X. Chen, M. Zhang, S. Li, L. Li, L. Zhang, T. Wang, M. Yu, Z. Mou, C. Wang, *J. Mater. Chem. B* **2017**, *5*, 1772.

[100] Y. Da Zhu, S. P. Chen, H. Zhao, Y. Yang, X. Q. Chen, J. Sun, H. S. Fan, X. D. Zhang, *ACS Appl. Mater. Interfaces* **2016**, *8*, 34209.

[101] B. Lü, Y. Chen, P. Li, B. Wang, K. Müllen, M. Yin, *Nat. Commun.* **2019**, *10*, 767.

[102] X. Xie, K. Jiang, B. Li, S. Hou, H. Tang, B. Shao, Y. Ping, Q. Zhang, *Biomaterials* **2022**, *286*, 121598.

[103] X. Li, D. Xi, M. Yang, W. Sun, X. Peng, J. Fan, *Adv. Healthcare Mater.* **2021**, *10*, 2101008.

[104] Y. Yang, W. Zhu, Z. Dong, Y. Chao, L. Xu, M. Chen, Z. Liu, *Adv. Mater.* **2017**, *29*, 1703588.

[105] S. S. Lucky, K. C. Soo, Y. Zhang, *Chem. Rev.* **2015**, *115*, 1990.

[106] X. Dai, T. Du, K. Han, *ACS Biomater. Sci. Eng.* **2019**, *5*, 6342.

[107] D. Wang, H. Wu, G. Yang, C. Qian, L. Gu, H. Wang, W. Zhou, J. Liu, Y. Wu, X. Zhang, H. Chen, D. Jana, Z. Guo, Y. Zhao, *ACS Nano* **2020**, *14*, 13500.

[108] S. Y. Yin, G. Song, Y. Yang, Y. Zhao, P. Wang, L. M. Zhu, X. Yin, X. B. Zhang, *Adv. Funct. Mater.* **2019**, *29*, 1901417.

[109] X. Zheng, L. Wang, Y. Guan, Q. Pei, J. Jiang, Z. Xie, *Biomaterials* **2020**, *235*, 119792.

[110] W. Liu, L. Chen, L. Wang, Z. Xie, *Adv. Mater. Interfaces* **2020**, *7*, 2000504.

[111] W. Zhang, B. Li, W. Duan, X. Yao, X. Lu, S. Li, Y. Tian, D. Li, *Inorg. Chem. Front.* **2022**, *9*, 670.

[112] P. Agostinis, K. Berg, K. A. Cengel, T. H. Foster, A. W. Girotti, S. O. Gollnick, S. M. Hahn, M. R. Hamblin, A. Juzeniene, D. Kessel, M. Korbelik, J. Moan, P. Mroz, D. Nowis, J. Piette, B. C. Wilson, J. Golab, *CA Cancer J. Clin.* **2011**, *61*, 250.

[113] A. P. Castano, T. N. Demidova, M. R. Hamblin, *Photodiagnosis Photodyn. Ther.* **2004**, *1*, 279.

[114] B. Li, H. Cao, J. Zheng, B. Ni, X. Lu, X. Tian, Y. Tian, D. Li, *ACS Appl. Mater. Interfaces* **2021**, *13*, 9739.

[115] D. Wang, H. Wu, C. Wang, L. Gu, H. Chen, D. Jana, L. Feng, J. Liu, X. Wang, P. Xu, Z. Guo, Q. Chen, Y. Zhao, *Angew. Chem. Int. Ed.* **2021**, *60*, 3001.

[116] D. Wang, H. Wu, W. Q. Lim, S. Z. F. Phua, P. Xu, Q. Chen, Z. Guo, Y. Zhao, *Adv. Mater.* **2019**, *31*, 1901893.

[117] W. Cai, H. Gao, C. Chu, X. Wang, J. Wang, P. Zhang, G. Lin, W. Li, G. Liu, X. Chen, *ACS Appl. Mater. Interfaces* **2017**, *9*, 2040.

[118] Y. Li, J. Tang, L. He, Y. Liu, Y. Liu, C. Chen, Z. Tang, *Adv. Mater.* **2015**, *27*, 4075.

[119] W. Shang, C. Zeng, Y. Du, H. Hui, X. Liang, C. Chi, K. Wang, Z. Wang, J. Tian, *Adv. Mater.* **2017**, *29*, 1604381.

[120] C. Hou, D. Zhao, Y. Wang, S. Zhang, S. Li, *J. Electroanal. Chem.* **2018**, *822*, 50.

[121] Y. Yuan, J. Xia, F. Zhang, Z. Wang, Q. Liu, *J. Electroanal. Chem.* **2018**, *824*, 147.

[122] Z. Qiu, T. Yang, R. Gao, G. Jie, W. Hou, *J. Electroanal. Chem.* **2019**, *835*, 123.

[123] T. Qian, C. Yu, X. Zhou, P. Ma, S. Wu, L. Xu, J. Shen, *Biosens. Bioelectron.* **2014**, *58*, 237.

[124] S. A. Hira, M. Nallal, K. Rajendran, S. Song, S. Park, J. M. Lee, S. H. Joo, K. H. Park, *Anal. Chim. Acta* **2020**, *1118*, 26.

[125] H. H. Zeng, W. Bin Qiu, L. Zhang, R. P. Liang, J. D. Qiu, *Anal. Chem.* **2016**, *88*, 6342.

[126] A. Ali, A. Alzamly, Y. E. Greish, M. Bakiro, H. L. Nguyen, S. T. Mahmoud, *ACS Omega* **2021**, *6*, 17690.

[127] S. Sachdeva, S. J. H. Koper, A. Sabetghadam, D. Soccol, D. J. Gravesteijn, F. Kapteijn, E. J. R. Sudhölter, J. Gascon, L. C. P. M. De Smet, *ACS Appl. Mater. Interfaces* **2017**, *9*, 24926.

[128] S. M. Sheta, S. M. El-Sheikh, D. I. Osman, A. M. Salem, O. I. Ali, F. A. Harraz, W. G. Shousha, M. A. Shoeib, S. M. Shawky, D. D. Dionysiou, *Dalton Trans.* **2020**, *49*, 8918.

[129] L. Chen, X. Wang, W. Lu, X. Wu, J. Li, *Chem. Soc. Rev.* **2016**, *45*, 2137.

[130] B. Yang, H. Gong, C. Chen, X. Chen, C. Cai, *Biosens. Bioelectron.* **2017**, *87*, 679.

[131] L. Wang, K. Liang, W. Feng, C. Chen, H. Gong, C. Cai, *Microchem. J.* **2021**, *164*, 106047.

[132] A. Gupta, S. K. Sharma, V. Pachauri, S. Ingebrandt, S. Singh, A. L. Sharma, A. Deep, *RSC Adv.* **2021**, *11*, 2167.

[133] M. L. Yola, N. Atar, *Nanoscale* **2020**, *12*, 19824.

[134] C. Cao, W. Ge, J. Yin, D. Yang, W. Wang, X. Song, Y. Hu, J. Yin, X. Dong, *Small* **2020**, *16*, 2000436.

[135] G. Franci, A. Falanga, S. Galdiero, L. Palomba, M. Rai, G. Morelli, M. Galdiero, *Molecules* **2015**, *20*, 8856.

[136] N. Bala, S. Saha, M. Chakraborty, M. Maiti, S. Das, R. Basu, P. Nandy, *RSC Adv.* **2015**, *5*, 4993.

[137] H. Agarwal, S. Menon, S. Venkat Kumar, S. Rajeshkumar, *Chem. Biol. Interact.* **2018**, *286*, 60.

[138] T. Mocan, C. T. Matea, T. Pop, O. Mosteanu, A. D. Buzoianu, S. Suciu, C. Puia, C. Zdrehus, C. Iancu, L. Mocan, *Cell. Mol. Life Sci.* **2017**, *74*, 3467.

[139] L. Rizzello, P. P. Pompa, *Chem. Soc. Rev.* **2014**, *43*, 1501.

[140] Z. Liu, J. Ye, A. Rauf, S. Zhang, G. Wang, S. Shi, G. Ning, *Biomater. Sci.* **2021**, *9*, 3851.

[141] X. Fan, F. Yang, J. Huang, Y. Yang, C. Nie, W. Zhao, C. Cheng, C. Zhao, R. Haag, *Nano Lett.* **2019**, *19*, 5885.

[142] Y. Yang, Y. Deng, J. Huang, X. Fan, C. Cheng, C. Nie, L. Ma, W. Zhao, C. Zhao, *Adv. Funct. Mater.* **2019**, *29*, 1900143.

[143] B. H. Neufeld, M. J. Neufeld, A. Lutzke, S. M. Schweickart, M. M. Reynolds, *Adv. Funct. Mater.* **2017**, *27*, 1702255.

[144] M. Chatterjee, C. P. Anju, L. Biswas, V. A. Kumar, C. G. Mohan, R. Biswas, *Int. J. Med. Microbiol*. **2016**, 306, 48.

[145] G. W. Peterson, D. T. Lee, H. F. Barton, T. H. Epps, G. N. Parsons, *Nat. Rev. Mater.*

2021, *6*, 605.

[146] W. L. Teo, J. Liu, W. Zhou, Y. Zhao, *SmartMat* **2021**, *2*, 567.

[147] J. Yao, Y. Cheng, M. Zhou, S. Zhao, S. Lin, X. Wang, J. Wu, S. Li, H. Wei, *Chem. Sci.* **2018**, *9*, 2927.

[148] W. Ma, J. Mao, X. Yang, C. Pan, W. Chen, M. Wang, P. Yu, L. Mao, Y. Li, *Chem. Commun.* **2019**, *55*, 159.

[149] K. Li, J. Yang, J. Gu, *Chem. Mater.* **2021**, *33*, 2198.

[150] Y. Kang, C. Xu, L. Meng, X. Dong, M. Qi, D. Jiang, *Bioact. Mater.* **2022**, *18*, 26.

[151] Y. Zhang, S. Yuan, X. Feng, H. Li, J. Zhou, B. Wang, *J. Am. Chem. Soc.* **2016**, *138*, 5785.

[152] P. Li, S. Y. Moon, M. A. Guelta, S. P. Harvey, J. T. Hupp, O. K. Farha, *J. Am. Chem. Soc.* **2016**, *138*, 8052.

[153] Q. Fu, L. Wen, L. Zhang, X. Chen, D. Pun, A. Ahmed, Y. Yang, H. Zhang, *ACS Appl. Mater. Interfaces* **2017**, *9*, 33979.

[154] R. Zhao, X. Shi, T. Ma, H. Rong, Z. Wang, F. Cui, G. Zhu, C. Wang, *ACS Appl. Mater. Interfaces* **2021**, *13*, 755.

[155] M. Pejman, M. Dadashi Firouzjaei, S. Aghapour Aktij, E. Zolghadr, P. Das, M. Elliott, M. Sadrzadeh, M. Sangermano, A. Rahimpour, A. Tiraferri, *Chem. Eng. J.* **2021**, *426*, 130704.

[156] Z. Wang, J. Wang, M. Li, K. Sun, C. J. Liu, *Sci. Rep.* **2014**, *4*, 5939.

[157] L. Gao, C. Y. V. Li, K. Y. Chan, *Chem. Mater.* **2015**, *27*, 3601.

[158] D. T. Sun, L. Peng, W. S. Reeder, S. M. Moosavi, D. Tiana, D. K. Britt, E. Oveisi, W. L. Queen, *ACS Cent. Sci.* **2018**, *4*, 349.

[159] S. Yang, L. Peng, O. A. Syzgantseva, O. Trukhina, I. Kochetygov, A. Justin, D. T. Sun, H. Abedini, M. A. Syzgantseva, E. Oveisi, G. Lu, W. L. Queen, *J. Am. Chem. Soc.* **2020**, *142*, 13415.

[160] D. T. Sun, N. Gasilova, S. Yang, E. Oveisi, W. L. Queen, *J. Am. Chem. Soc.* **2018**, *140*, 16697.

Table of Contents Graphic

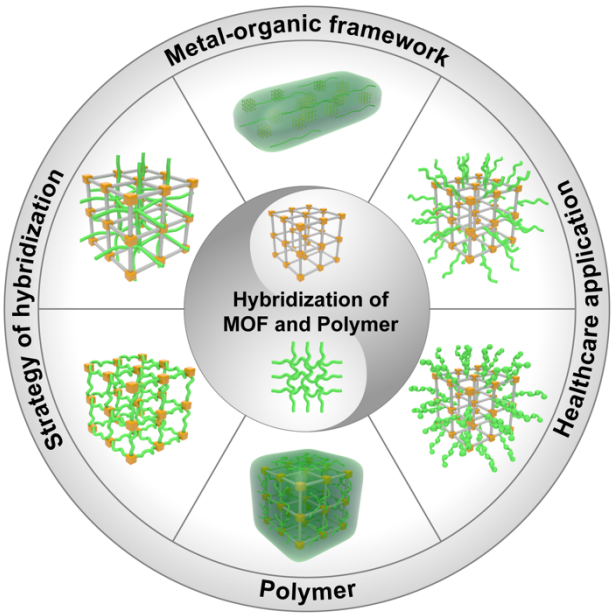

Hybridizing metal-organic frameworks (MOFs) with flexible polymers leads to unique properties wherein the incorporation of suitable polymers enhances the MOF performance. This review highlights the recent advances in the preparation of MOF-polymer nanomaterials, and discusses their applications in anticancer, anti-bacteria, imaging, protection from oxidative stress and inflammation, and environmental remediation. Insights from the current research and design principles for addressing future challenges are revealed.